

LA-UR-17-21696 (Accepted Manuscript)

# Compatible, energy conserving, bounds preserving remap of hydrodynamic fields for an extended ALE scheme

Burton, Donald E. Morgan, Nathaniel Ray Charest, Marc Robert Joseph Kenamond, Mark Andrew Fung, Jimmy

Provided by the author(s) and the Los Alamos National Laboratory (2018-03-19).

To be published in: Journal of Computational Physics

**DOI to publisher's version:** 10.1016/j.jcp.2017.11.017

Permalink to record: http://permalink.lanl.gov/object/view?what=info:lanl-repo/lareport/LA-UR-17-21696

#### Disclaimer:

Approved for public release. Los Alamos National Laboratory, an affirmative action/equal opportunity employer, is operated by the Los Alamos National Security, LLC for the National Nuclear Security Administration of the U.S. Department of Energy under contract DE-AC52-06NA25396. Los Alamos National Laboratory strongly supports academic freedom and a researcher's right to publish; as an institution, however, the Laboratory does not endorse the viewpoint of a publication or guarantee its technical correctness.



# Accepted Manuscript

Compatible, energy conserving, bounds preserving remap of hydrodynamic fields for an extended ALE scheme

D.E. Burton, N.R. Morgan, M.R.J. Charest, M.A. Kenamond, J. Fung

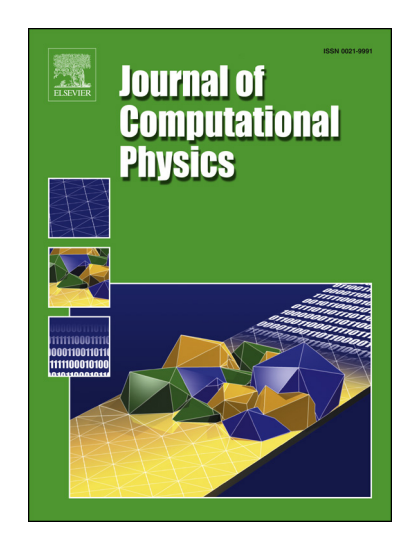
PII: S0021-9991(17)30855-0

DOI: https://doi.org/10.1016/j.jcp.2017.11.017

Reference: YJCPH 7716

To appear in: Journal of Computational Physics

Received date: 9 March 2017 Revised date: 16 October 2017 Accepted date: 13 November 2017



Please cite this article in press as: D.E. Burton et al., Compatible, energy conserving, bounds preserving remap of hydrodynamic fields for an extended ALE scheme, *J. Comput. Phys.* (2017), https://doi.org/10.1016/j.jcp.2017.11.017

This is a PDF file of an unedited manuscript that has been accepted for publication. As a service to our customers we are providing this early version of the manuscript. The manuscript will undergo copyediting, typesetting, and review of the resulting proof before it is published in its final form. Please note that during the production process errors may be discovered which could affect the content, and all legal disclaimers that apply to the journal pertain.

### Highlights

- The context is ALE remap between grids of potentially dissimilar connectivity.
- A new higher order, center of mass (CM) reconstruction method is presented.
- CM reconstruction is shown to be superior to the traditional centroidal reconstruction.
- A new "compatible" (CE) method for conservatively remapping energy is derived.
- CE is shown to be better than common total and internal energy conserving methods.

## Compatible, energy conserving, bounds preserving remap of hydrodynamic fields for an extended ALE scheme

D.E. Burton<sup>a,\*</sup>, N. R. Morgan<sup>a</sup>, M.R.J. Charest<sup>a</sup>, M.A. Kenamond<sup>a</sup>, J. Fung<sup>a</sup>

<sup>a</sup>X-Computational Physics Division; Los Alamos National Laboratory; P.O. Box 1663, Los Alamos, NM, USA

#### **Abstract**

From the very origins of numerical hydrodynamics in the Lagrangian work of von Neumann and Richtmyer [83], the issue of total energy conservation as well as entropy production has been problematic. Because of well known problems with mesh deformation, Lagrangian schemes have evolved into Arbitrary Lagrangian-Eulerian (ALE) methods [39] that combine the best properties of Lagrangian and Eulerian methods. Energy issues have persisted for this class of methods. We believe that fundamental issues of energy conservation and entropy production in ALE require further examination.

The context of the paper is an ALE scheme that is *extended* in the sense that it permits cyclic or periodic remap of data between grids of the same or differing connectivity. The principal design goals for a remap method then consist of total energy conservation, bounded internal energy, and compatibility of kinetic energy and momentum. We also have secondary objectives of limiting velocity and stress in a non-directional manner, keeping primitive variables monotone, and providing a higher than second order reconstruction of remapped variables.

In particular, the new contributions fall into three categories associated with: energy conservation and entropy production, reconstruction and bounds preservation of scalar and tensor fields, and conservative remap of nonlinear fields. The paper presents a derivation of the methods, details of implementation, and numerical results for a number of test problems. The methods requires volume integration of polynomial functions in polytopal cells with planar facets, and the requisite expressions are derived for arbitrary order.

Keywords: Lagrangian, hydrodynamics, remap, energy conserving, bounds preserving, mimetic, cell-centered, ALE, exact intersection, KE fixup, finite-volume

#### 1. Introduction

From the very origins of numerical hydrodynamics in the Lagrangian work of von Neumann and Richtmyer [83], the issue of total energy conservation as well as entropy production has been problematic. Only in recent years have methods for conserving energy within the traditional spatially staggered Lagrange framework (SGH) become widespread. The lack of conservation was a consequence of staggered differencing in which internal energy naturally resided in the cell and kinetic energy at the nodes. The earliest work in 1D was due to Trulio and Trigger [77]. Conservation in the multi-dimensional SGH framework was eventually enabled by the development of so-called compatible energy hydro schemes [11, 10, 13, 12, 23]. In the last decade, cell-centered Lagrangian schemes (CCH) based on Godunov methods have appeared that naturally conserve total energy [29, 57, 16].

Because of well known problems with mesh deformation, Lagrangian schemes have since evolved into Arbitrary Lagrangian-Eulerian (ALE) methods [39] that combine the best properties of Lagrangian and Eulerian methods. Traditional ALE schemes *advect* material only between adjacent cells within a mesh that is incrementally adapted. The context of the paper is an *extended ALE* scheme that permits cyclic or periodic transfer of data between grids of the *same or differing connectivity*. Viewed in detail, the ALE procedure involves: (a) a Lagrange step, (b) mesh optimization, (c) determination of intersection volumes, (d) reconstruction of fields within donor cells, (e) a conservative

<sup>\*</sup>Corresponding author: burton@lanl.gov

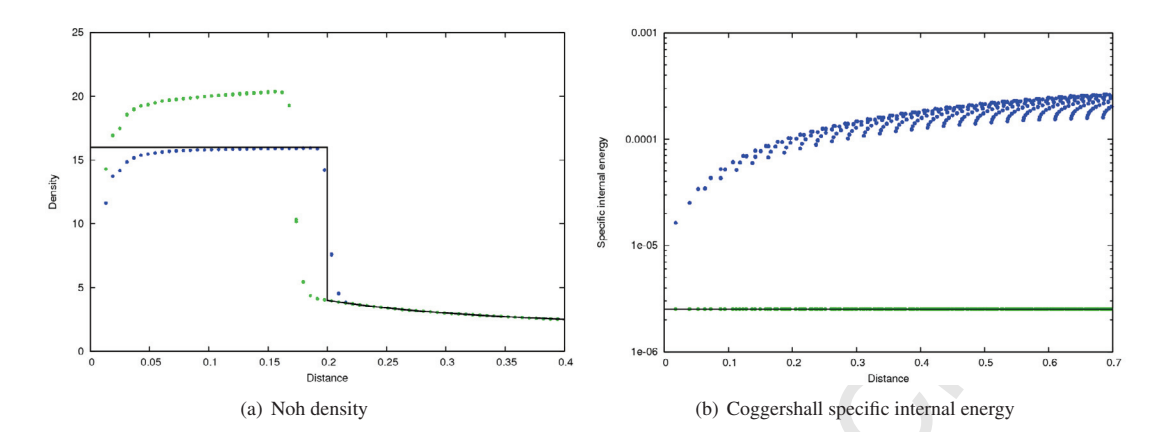


Figure 1: Scatter plots for two ALE test problems that are discussed in detail later. Both simulations used a polar mesh. Figure (a) shows density vs. distance for the Noh problem (Section 6.1.2) at t=0.6. The figure compares results from an internal energy (IE) conserving method (green) and a total energy (TE) conserving method (blue) with the analytic solution (black). Figure (b) shows specific internal energy on a logarithmic scale vs. distance for the Coggeshall problem (Section 6.2.2) at t=0.5. Again, the same IE and TE methods are compared with the analytic results. However, in (a), the TE method yields the best result, while in (b), the IE result is best. These calculations used a reconstruction method (designated CM) discussed later.

remap, and finally (f) a repartition of kinetic and internal energy in acceptor cells. Although the overall context is more general, the focus of this paper is on the physics and numerics of the reconstruction (d) through repartition steps (f). In particular, the new contributions fall into three categories associated with: energy conservation and entropy production, reconstruction and bounds preservation of scalar and tensor fields, and conservative remap of nonlinear fields.

#### 1.1. Energy and entropy remap

We believe that fundamental issues of energy conservation and entropy production have persisted for ALE methods and require further examination. Although total energy conservation is numerically straightforward, the literature addressing entropy production in ALE is sparse. We examine the fundamental entropy issues in Section 5. Although we discuss entropy production in a conceptual sense, entropy itself is not usually calculated. Rather, we use the term to imply the dissipation of kinetic energy into internal energy.

Internal energy (IE) method. Early ALE, as well as Eulerian codes, were based on SGH and typically conserved momentum and internal energy, but not total energy, just as the Lagrangian codes did. In CCH as well as SGH, this can cause entropy errors that affect shock states and propagation velocities as demonstrated in test problems such as the Noh problem [63, 18].

*Total energy (TE) method.* An alternative strategy is to conservatively remap the total energy and calculate the internal energy by subtracting kinetic energy from the total energy. Total energy conserving methods can produce significant errors in problems involving isentropic flows such as the Coggeshall problem [27].

The calculations presented in Figure 1 as well as all figures throughout the paper were carried out with the same underlying code [14] with only algorithmic components varied. The Noh and Coggeshall problems will be discussed in more detail in Sections 6.1.2 and 6.2.2. Here, we present a preview to highlight the energy issue. We use a center of mass reconstruction scheme described in the next section. Figure 1(a) compares results from the Noh problem using an IE method with a TE method. The IE method is not conservative, produces a slow propagation velocity and overshot the shock state, while the TE method matches the arrival and plateau quite well. Both methods show the expected wall heating near the origin [63]. Figure 1(b) is a scatter plot of specific internal energy vs. distance for the Coggeshall problem and again compares the IE and TE methods. In contrast to the Noh problem, the IE method gives the correct solution (uniform across the mesh), while the TE method is in error by nearly two orders of magnitude because of excess heating during remap.

The point, of course, is that neither IE nor TE methods solve both shock and smooth flow problems. In Section 5, we derive a new *compatible energy (CE)* method that resolves the energy issues.

KE fixup method. A quasi-total energy scheme called KE fixup is attributed to Roger DeBar [28]. The method is discussed by Benson [5] and is also mentioned in [42], but is otherwise not well documented. The underlying principle of KE fixup is based on algorithmic choice rather than fundamental physical principle. The method tries to synchronize the advected cell kinetic energy K with the cell average momentum  $U^2/2M$ . Enforcement of total energy conservation then requires an adjustment in the internal energy. The adjustment is accomplished by calculating a quantity

$$Q = K - \frac{\mathbf{U}^2}{2M}$$

that is the difference between advected kinetic energy K and kinetic energy inferred from the momentum equation. Q is then added selectively to the advected internal energy and subtracted from the kinetic energy. Note that Q is an energy and not an artificial viscosity.

By adding Q in shocks, but not in smooth flows, the entropy error in smooth flows is avoided. The scheme is sensitive to the shock detection criterion. Without the selective application of Q, this would be a total energy scheme since both internal and kinetic energy would be conserved. However, with the selective application, the scheme does not completely enforce conservation of total energy.

Our CE method bears some similarity to *KE fixup*, but in Section 5, we re-examine the aforementioned underlying principle and reach differing conclusions.

#### 1.2. Reconstruction

In the reconstruction step, conserved quantities are redistributed within the cell. The redistribution is constrained to avoid producing local extrema within the vicinity of the cell. The methods of doing this are of three basic types: *a priori* methods of van Leer [78, 79] and Barth and Jespersen [3, 2] that limit gradients in the donor cells; *a posteriori* procedures such as the repair scheduledme of Shashkov and Wendroff [72] that correct the acceptor cells; and intermediate methods that modify the fluxes, such as the sign preserving scheme of Margolin and Shashkov [59] and flux corrected transport (FCT) [7, 86, 50].

Following common terminology, we refer to intensive quantities as *primitive* variables. We further classify specific variables (per mass) as *mass-weighted*, and generalized densities (per volume) as *volume-weighted*. Most *conserved* variables are volume-weighted products of density times some specific variable. Thus, a primitive specific variable  $\phi$  has a conserved counterpart  $\rho\phi$ .

Center of volume (CV) or centroidal reconstruction. In the remap, compatibility issues arise if relationships between variables are not maintained during the process, especially in reconstruction. The most commonly used a priori reconstructions distribute the density  $\rho$  and other conserved variables  $\rho\phi$  linearly through the centroid of the cell. The gradients of both are then limited to keep the distribution within local bounds. This gives rise to a compatibility error because the recomputed value of the specific variable  $\phi = (\rho\phi)/\rho$  is not necessarily within bounds of adjacent cells. This can produce negative internal energies, giving rise to imaginary sound speeds for some equations of state. It can also cause catastrophic instabilities, especially in problems with high speeds and low internal energy, and this was an issue driving the work of [58, 72].

The flux corrected transport (FCT) of Boris and Book [7, 86, 50] was extended by Schar and Smolarkiewicz [70] who used FCT to synchronize the limiters for  $\rho$  and  $\rho\phi$  such that the  $\phi$  was also bounded. Many variables can be synchronized with the density, but this tends to increase dissipation by forcing the density field toward first order. For CV reconstruction and internal energy conservation (IE), synchronization of density and only specific internal energy is the usual practice.

For CV reconstruction and total energy conservation (TE), the situation is yet more complicated. Internal energy is constrained to be the difference between total and kinetic energy. As the difference of two monotonic functions is not necessarily monotonic, this can give rise to instabilities [60, 1, 5, 18]. Historically, these instabilities have often been erroneously attributed to round off errors in subtracting two large numbers, but they actually result from truncation errors arising from incompatible numerical approximations used in calculating the total and kinetic energy. Such instabilities can appear in the smooth flow region of the Noh problem that is characterized by large kinetic energy and

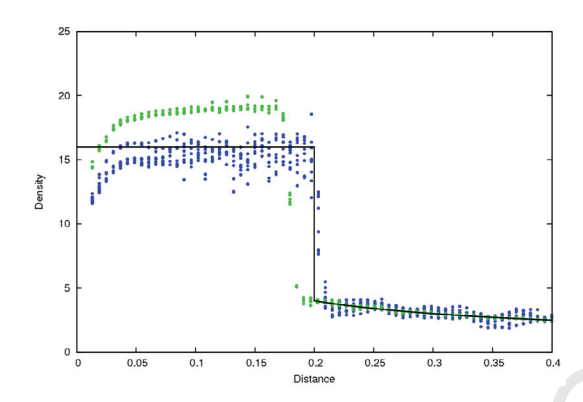


Figure 2: Scatter plots of density vs. distance for the Noh problem (Section 6.1.2) at t=0.6 using a box mesh. For CV reconstruction, the figure compares results from an internal energy (IE) conserving method (green) and a total energy (TE) conserving method (blue) with the analytic solution (black). Both IE and TE methods are noisy. These results should be compared with Figure 1(a) that used a CM reconstruction rather than CV.

low internal energy as exemplified in Figure 2. Such a scheme requires a more complicated approach because limiting must be synchronized for not only density and internal energy, but also velocity. Because of the additional variable, increased dissipation would be expected. Liska, Shashkov, Váchal, and Wendroff [53, 54] developed a flux-corrected scheme that synchronized limiters for density, internal energy, and velocity. In [80], it was found that the second order method was excessively dissipative and that results were improved by using third order.

Center of mass (CM) reconstruction. An alternative a priori solution to the synchronization problem was proposed in another context by Dukowicz and Baumgardner [32]. They distributed  $\rho$  linearly about the centroid, but  $\phi$  linearly about the center of mass, so that limiting was done with respect to the specific variable  $\phi$  rather than the conserved variable  $\rho\phi$ . Because  $\rho$  and  $\phi$  are linear functions, the product distribution  $\rho\phi$  is quadratic. The method was recently applied to the internal energy in an SGH ALE context by Kucharik and Shashkov [49]. CM reconstruction does guarantee that all specific quantities are bounded, avoiding the previously discussed instabilities. The difference between the CM and CV methods can be seen by comparing Figures 1(a) and 2.

We use the CM reconstruction method as derived in Section 3, but with an additional constraint on internal energy discussed in Section 3.1 that also guarantees the boundedness of the internal energy density  $\rho e$ . This makes a substantial improvement in the Sod problem of Section 6.1.1. As with the Schar and Smolarkiewicz method, applying this to additional variables can give rise to excessive dissipation.

#### 1.3. Advection vs. remap

Swept face advection. The most common method of determining the exchange volume in ALE calculates the volume swept out by the movement of a cell face. The method has the advantage of being simple, but has several distinct disadvantages. The time step is limited by the relative velocity of the fluid with respect to the mesh. Advection is only through surfaces, so there is no direct coupling across cell corners. It is possible for the swept volume to consist of a bowtie (a non-convex polygon), so there could be advection in opposing directions, making the centroid ill defined. Lastly, its use is restricted to meshes of the same connectivity.

Exact intersection remap. An alternative to swept face advection is remap that derives from the pioneering work of Dukowicz and collaborators [34, 67, 68, 35, 33] and uses the exact geometrical intersections of donor and acceptor meshes and surface integrals to calculate the quantities transferred. Unlike swept face advection, remap permits large mesh adjustments or even completely new meshes. It is not constrained to incremental movement of material through cell surfaces, thereby permitting large timesteps. Corner coupling is automatic, as is the handling of bowtie configurations. References [20, 17, 18, 43, 47] showed that the error can be significantly reduced by employing exact intersection remap methods in lieu of swept face methods. Remap also opens the door to mesh management strategies

such as periodic remeshing of Lagrangian meshes and the reconnection based Arbitrary Lagrangian Eulerian (ReALE) method [55, 6].

The relevance of the advection vs. remap issue to the current work is that the remap requirement places constraints on the formulation that would not be present in a swept-face scheme. That is, the formulation cannot rely upon logical relationships between old and new meshes.

#### 1.4. Design goals

The specific design goals for our compatible remap method then consist of the following.

Lagrange hydro. The context of this work is a remap method appropriate to cell-centered hydrodynamics (CCH) such as described in [29, 57, 16, 19]. To the extent possible, our intent is to avoid placing additional constraints on the underlying Lagrange method. An exception to this is the treatment of kinetic energy.

*Exact intersection remap.* The method must be able to remap between meshes of the same or differing connectivity. The geometry of the volumes of intersection must be determined by an exact intersection method. We note that, although the methods presented are formulated for an exact intersection scheme, they are also suitable for swept face methods without connectivity change.

Conservation. Quantities conserved in the Lagrange equations, especially total energy, must be conserved in the remap.

Compatibility. Hydrodynamic variables are interrelated in the Lagrange step, and the remap must preserve these relationships. In particular, the partition of kinetic and internal energy at the point at which the constitutive model is applied should be compatible with the velocity at that point.

*Entropy production.* In addition to conservation of total energy and boundedness of internal energy, the formulation must include an entropy production mechanism that tends to synchronize kinetic energy and momentum. In particular, the mechanism should produce entropy in shocks, but not in isentropic flows.

*Reconstruction.* The reconstruction of conserved quantities must be second order or greater.

*Bounds*. Primitive variables corresponding to quantities conserved in the Lagrange equations must be bounded by the cell averages in adjacent cells. In particular, the specific internal energy must be bounded. Further, vector and tensor variables must be bounded in a non-directional manner.

#### 1.5. Omissions

As the focus of this paper is on the physics and numerics of the remap, the following topics, that are important components of a fully functional ALE code, will be discussed only briefly.

*Geometry*. Although we consider only 2D XY geometry in the test problems, we derive the conservation integrals for 3D as well as 2D XY and RZ in Appendix B.

*Mesh intersections*. A number of methods are available for determining the geometry of the intersecting volumes of polytopal cells. For details, see [34, 33, 18, 43, 49, 26, 37, 36] .

*Mesh optimization.* Discussion of various mesh optimization strategies is well beyond the scope of the paper, aside from what is necessary to explain the test problems of Section 6.

*Mixtures and multi-material cells.* Similarly, while important in ALE schemes, description of interface reconstruction methods is also beyond the scope of the paper, as are closure models.

Constitutive models. As the focus of this work is remap and not constitutive formulations, the development is directed toward hypo elastic/plastic formulations such as that of Wilkins [85].

#### 1.6. Notation

*Intensive and extensive quantities.* Extensive quantities (that depend upon how much of something is present) are indicated by capital letters, while intensive ones are lower case. For example, *k* is the specific kinetic energy and *K* is the kinetic energy in a particular control volume.

Superscripts and subscripts. Superscripts will be used principally to indicate spatial location. Donor and acceptor cells are denoted A and B respectively, whereas I denotes a volume of intersection between donor and acceptor. Upper case  $\{A, B, I\}$  refer to the center of mass (CM), whereas, lower case  $\{a, b, i\}$  refer to the centroid.

Scalars, vectors, tensors. Where typographic fonts permit, vectors and tensors will be bold faced, and scalars not. Scalar products are indicated by a dot, such as  $\hat{\mathbf{n}} \cdot \sigma \leftrightarrow \hat{n}_i \sigma_{ii}$ . Dyadic tensors are indicated by juxtaposition  $\hat{\mathbf{n}} \mathbf{u} \leftrightarrow \hat{n}_i u_i$ . The double scalar product is expressed  $\sigma: \mathbf{G} \leftrightarrow \sigma_{ii}G_{ii}$ .

#### 1.7. Organization of the paper

The organization of the paper is as follows. The Lagrange step is summarized in Section 2, and Section 2.2 describes alternatives for partitioning of total energy into kinetic and internal components. A new method for reconstructing fields within donor cells is discussed in Section 3.1 describes procedures for limiting gradients of scalars and vectors, as well as a new method for tensors. A new method for conservatively remapping higher order polynomial fields is presented in Section 4.1. A new perspective on entropy production and repartitioning of energy after remap is discussed in Section 5. The results of a number of test problems are given in Section 6. Our conclusions are summarized in Section 7. Appendix A discusses polynomial integration. Appendix B presents previously unpublished equations for 2D and 3D moment integrals of higher order polynomial functions for polytopal volumes.

#### 2. Lagrange formulation

We begin with the Lagrange equations that are taken from [16] but are typical of cell-centered formulations. The equations are not solved here, but are summarized to introduce notation, to call attention to conservation requirements, and to point out key assumptions in the partitioning of kinetic and internal energy. In particular, the section calls attention to the usual practice of inferring the kinetic energy from the momentum equation as  $U^2/2M$  instead of explicitly integrating it. As discussed in Section 5, this is a critical point relating to entropy production in remap.

#### 2.1. Finite volume equations

The extensive conserved quantities are volume V, mass M, deformation G, momentum U, and total energy H. The rate equations for these are surface integrals are

$$\dot{M} = 0 \tag{1}$$

$$\dot{\mathbf{G}} = M\dot{\mathbf{g}} = \oint d\mathbf{N} \,\mathbf{u} \tag{2}$$

$$\dot{\mathbf{U}} = M\dot{\mathbf{u}} = \oint d\mathbf{N} \cdot \boldsymbol{\sigma} \tag{3}$$

$$\dot{\mathbf{G}} = M\dot{\mathbf{g}} = \oint d\mathbf{N} \,\mathbf{u} \tag{2}$$

$$\dot{\mathbf{U}} = M\dot{\mathbf{u}} = \oint d\mathbf{N} \cdot \boldsymbol{\sigma} \tag{3}$$

$$\dot{H} = M\dot{h} = \oint d\mathbf{N} \cdot \boldsymbol{\sigma} \cdot \mathbf{u} \tag{4}$$

in which dN is a normal surface vector, **u** is the surface velocity, and the quantity  $\sigma$  is the Cauchy stress tensor. The rates for the preceding conserved quantities are temporally integrated, for example,

$$H = \int dt \, \dot{H}$$

The corresponding cell averages are given by h = H/M or, in the case of density, by  $\rho = M/V$ . As discussed later in an ALE context, the mass density will be associated with an integration point at the cell centroid and the specific quantities will be associated with the cell center of mass.

Deformation. The quantity **g** represents a conserved Lagrangian measure of the deformation rate. The normalization is largely a matter of convention. We have chosen to normalize per unit mass to maintain compatibility with the volume equation that is simply the trace of the deformation equation

$$\dot{V} = M\dot{v} = \oint d\mathbf{N} \cdot \mathbf{u} = tr(\dot{\mathbf{G}})$$
 (5)

Another common convention defines volumetric strain per some constant reference volume. The difference between the two forms is taken up by a constant density factor in the constitutive model. As a third variation, in hypo elastic models [85], the left hand side of the deformation equation is normalized per current volume to yield the discrete form of the velocity gradient, that is a non-conservative measure of deformation. The velocity gradient is related to the preceding deformation rate by

$$\nabla \mathbf{u} = \rho \dot{\mathbf{g}}$$

The symmetrized deformation rate tensor is

$$\dot{\mathbf{F}} = M \, \dot{\mathbf{f}} = \frac{1}{2} \left( \dot{\mathbf{G}} + \dot{\mathbf{G}}^T \right)$$

In the discrete implementation of the volume equation (5), it is important to enforce volumetric compatibility, also known as the Geometric Conservation Law (GCL) [76, 75, 84, 56]. That is, the volume change of a cell, calculated from the surface integral (5), must algebraically equal that determined from the volume change calculated from the displacement of the bounding nodes. The Lagrange scheme discussed here has been shown to satisfy the GCL in Cartesian [16] and axisymmetric [15] geometry.

#### 2.2. Energy partitioning

Partitioning of total energy into kinetic and internal components is part of the Lagrange step, but is not formally part of the finite volume methodology. Energy is partitioned into kinetic and internal components solely to obtain specific internal energy at an integration point  $\mathbf{x}$  for use in a constitutive model. This partitioning can be accomplished in two different ways.

Canonical partitioning. In a canonical method that is used in SGH [11, 10, 13, 12, 23] and many of the CCH compatible energy schemes [29, 57], the total energy is first integrated in time

$$H = \int dt \, \dot{H}$$

The cell kinetic energy at time n is assumed to be compatible with the extensive cell momentum  $U^n$  and is given by

$$K^n = \frac{(\mathbf{U}^n)^2}{2M} \tag{6}$$

Then, the change during the time step is given exactly by

$$\Delta K = \frac{1}{2M} \left[ \left( \mathbf{U}^{n+1} \right)^2 - \left( \mathbf{U}^n \right)^2 \right] \tag{7}$$

$$= \frac{1}{2M} \left( \mathbf{U}^{n+1} - \mathbf{U}^n \right) \cdot \left( \mathbf{U}^{n+1} + \mathbf{U}^n \right) \tag{8}$$

$$= \left(\dot{\mathbf{U}}\delta t\right) \cdot \bar{\mathbf{u}} \tag{9}$$

in which  $\delta t$  is the timestep and  $\bar{\mathbf{u}}$  is the temporal average velocity

$$\bar{\mathbf{u}} = \frac{1}{2} \left( \mathbf{u}^{n+1} + \mathbf{u}^n \right) \tag{10}$$

The integrated internal energy is then given exactly by

$$E = H - K$$

As kinetic energy is a function of the cell momentum in the canonical partitioning, it does not need to be explicitly integrated. This partitioning further assumes that the specific kinetic and internal energies at the integration point  $\mathbf{x}$  are

$$k\left(\mathbf{x}\right) = K/M\tag{11}$$

$$e\left(\mathbf{x}\right) = E/M\tag{12}$$

The specific internal energy is then an input to the constitutive model that is evaluated at the point x.

As we will show in Section 5, the extensive kinetic energy as defined in (6) is the cause of overheating in isentropic flows, such as the Coggeshall problem of Section 6.2.2. This observation suggests the alternative rate based partitioning discussed next.

Rate based partitioning. Unlike the canonical partitioning, the rate based partitioning described here does not assume the cell kinetic energy is given by  $U^2/2M$ . Rather, it is a time integral, requiring an additional history variable. In a pure Lagrange calculation, the cell kinetic energy will be exactly given by  $U^2/2M$  as in the canonical method, but this will not be the case in ALE calculations.

The partitioning of the total energy into its various components was derived in [16]. After some manipulation and making use of the momentum and deformation equations, the evolution equation for total energy can be written

$$\dot{H} = \oint d\mathbf{N} \cdot \boldsymbol{\sigma} \cdot \mathbf{u} \tag{13}$$

$$= \left\{ \begin{array}{l} \left[ \oint d\mathbf{N} \cdot \sigma \right] \cdot \bar{\mathbf{u}} \\ + \left[ d\mathbf{N} \, \mathbf{u} \right] : \bar{\sigma} \\ + \left[ \oint d\mathbf{N} \cdot (\sigma - \bar{\sigma}) \cdot (\mathbf{u} - \bar{\mathbf{u}}) \right] \end{array} \right\}$$
(14)

$$= \dot{\mathbf{U}} \cdot \bar{\mathbf{u}} + \dot{\mathbf{G}} : \bar{\sigma} + \dot{Q} \tag{15}$$

$$= \dot{K} + \dot{W} + \dot{Q} \tag{16}$$

in which the rate equations for kinetic energy, reversible work, and dissipation are given respectively by

$$\dot{K} = \dot{\mathbf{U}} \cdot \bar{\mathbf{u}} \tag{17}$$

$$\dot{W} = \dot{\mathbf{G}} : \bar{\sigma} \tag{18}$$

$$\begin{aligned}
\dot{K} &= \mathbf{U} \cdot \mathbf{u} & (17) \\
\dot{W} &= \dot{\mathbf{G}} : \bar{\sigma} & (18) \\
\dot{Q} &= \oint d\mathbf{N} \cdot (\sigma - \bar{\sigma}) \cdot (\mathbf{u} - \bar{\mathbf{u}}) & (19)
\end{aligned}$$

The quantity  $\bar{\sigma}$  is a time centered stress tensor, while  $\bar{\bf u}$  is as defined in (10). A dissipation relation between  $\sigma$  and  $\bf u$ guarantees that  $\dot{Q}$  is always positive. Note that rate based partitioning uses the same equation for the change in kinetic energy as does the canonical method (9).

The internal energy rate is that part of the total energy not associated with the bulk flow, so that

$$\dot{E} = \dot{H} - \dot{K} \tag{20}$$

It is also true that

$$\dot{E} = \dot{W} + \dot{Q}$$

but this relation is not actually used because the internal energy can be obtained from (20), so that it is not necessary to explicitly calculate  $\dot{W}$  or  $\dot{Q}$ . The total energy rate  $\dot{H}$  corresponds to the Hamiltonian, and the Lagrangian is the difference between the kinetic and internal energy  $\dot{L} = \dot{K} - \dot{E}$ . The effect of the dissipation is to reduce the Lagrangian until the flow is smooth.

In the partitioning described in [16], total, kinetic, and internal energy are all temporally integrated

$$H = \int dt \, \dot{H}$$

$$K = \int dt \, \dot{K}$$

$$E = \int dt \, (\dot{H} - \dot{K})$$

The internal energy is explicitly integrated to reduce numerical roundoff, but is formally E = H - K. As in canonical partitioning, the specific internal energy at the integration point is taken to be the cell average.

Linearized kinetic energy. There is an incompatibility in the CCH Lagrange formulation regarding the velocity distribution. A linear velocity field is assumed in the second-order CCH reconstruction, corresponding to a quadratic kinetic energy distribution. However, in the two energy partitionings (9) and (17), the velocity field  $\bar{\bf u}$  is assumed to be uniform. This is a first order approximation that corresponds to a linear distribution of kinetic energy. This incompatibility has entropy implications that are discussed in detail in Section 5.

#### 2.3. Constitutive models

We focus on hypo elastic/plastic models that are heavily used in engineering applications, but note that they are not rigorously conservative. These models tend to be based upon the work of Wilkins [85]. The remap formulation can be readily adapted to hyper elastic/plastic models, but such is beyond the scope of this work. For an excellent discussion of hyper elasticity in the context of cell-centered hydrodynamics, see [48]. In hypo elastic models, the Lagrangian deformation tensor  $\mathbf{G}$  is not usually integrated. Instead, the symmetric strain rate tensor  $\dot{\mathbf{e}}$  and asymmetric spin tensor  $\dot{\mathbf{\omega}}$  are inferred from the Lagrangian deformation rate  $\dot{\mathbf{G}}$ . These are used in the constitutive model to correct for rotations and calculate a stress rate  $\dot{\sigma}$  that is temporally integrated to yield the Cauchy stress  $\sigma$ . We note that elastic deformation, and not stress, is a formally conserved quantity. However, as is usual in hypo elastic formulations, a pseudo conservation equation is invoked in Section 4, for stress in lieu of deformation,

$$\Sigma = V\sigma$$

The constitutive model may have an arbitrary number of additional variables that must be conserved, for example, plastic strain.

#### 3. Center of mass (CM) reconstruction

In the sequence of operations, the Lagrange step described in the previous section is followed by a mesh optimization step and then a reconstruction or redistribution step. The finite volume method provides no direct information regarding the distribution of conserved quantities, so that this information must be inferred from adjacent cells. In a second-order method, linear distributions are assumed for fields. Unlimited gradients are denoted  $\tilde{\nabla}$  and are obtained by a least squares fit to values in neighboring cells. These gradients are then limited as described later to assure monotonicity of the distributions, yielding limited gradients  $\nabla$ .

As discussed in Section 1, for specific variables  $\phi$ , the CV reconstruction method [70] linearizes the product  $\rho\phi$ , resulting in a remapped  $\phi$  field that is not necessarily monotonic. To avoid this problem, we employ the CM reconstruction method of Dukowicz and Baumgardner [32] that was mentioned in Section 1.2. We note that the CM method was recently applied to the internal energy in an SGH context in [49].

Suppose the mass in a donor cell A is described by a distribution  $\rho(\mathbf{x})$  such that the total mass in the cell is given by

$$M = \int dV \, \rho\left(\mathbf{x}\right)$$

The cell average mass density is  $\bar{\rho} = M/V$ . For a linear distribution, the density at the cell *centroid*  $\mathbf{x}^a$  (note lower case superscript) is equal to the cell volume average  $\rho^a \equiv \rho(\mathbf{x}^a) = \bar{\rho}$ .

Now, consider a specific quantity described by a distribution  $\phi(\mathbf{x})$  such that the extensive quantity in the cell is given by

$$\Phi = \int_{A} dV \, \rho(\mathbf{x}) \, \phi(\mathbf{x})$$

The mass average of the specific variable is  $\bar{\phi} = \Phi/M$ . For a linear distribution of a specific quantity, the value at the center of mass  $\mathbf{x}^A$  (note upper case superscript) is equal to the cell mass average  $\phi^A \equiv \phi\left(\mathbf{x}^A\right) = \bar{\phi}$ . Then

$$\Phi = M\phi\left(\mathbf{x}^A\right) \tag{21}$$

The linear distributions of  $\rho$  and other volume-weighted fields are relative to the centroid  $\mathbf{x}^{\mathbf{a}}$  while those for specific quantities  $\phi$  relative to the CM  $\mathbf{x}^{\mathbf{A}}$ 

$$\rho(\mathbf{x}) = \rho^a + (\mathbf{x} - \mathbf{x}^a) \cdot \nabla \rho \tag{22}$$

$$\phi(\mathbf{x}) = \phi^A + (\mathbf{x} - \mathbf{x}^A) \cdot \nabla \phi \tag{23}$$

The product  $\rho\phi$  is the corresponding conserved variable and is represented by a higher than second order polynomial.

#### 3.1. Limiters for remap

The monotonicity of the primitive distributions is achieved by limiting the gradients. Following Barth-Jespersen [3], we do this by guaranteeing that every point within the donor cell lies within the range of bounding cells. Our set of bounding cells includes all cells sharing common nodes, not simply those across cell faces. Using the unlimited gradients, we project to each corner of the donor cell and calculate a limiting factor such that the bounds are satisfied. See Figure 3 that illustrates projection from either the centroid (a) or the CM (A) to the corner of a donor cell.

For CV reconstruction, the same limiting method is commonly applied to both scalars as well as individual components of vectors and tensors. In the following CM reconstruction, however, different procedures are used depending upon whether fields are volume-weighted or mass-weighted or whether they are scalar, vector, or tensor fields. Further, special procedures are applied to the density and specific internal energy.

Density. Consider first, the mass density  $\rho$ . The distance from the cell centroid  $\mathbf{x}^a$  to a point on the cell boundary  $\mathbf{x}^p$  is  $\mathbf{x}^{pa} = \mathbf{x}^p - \mathbf{x}^a$ . The unlimited density difference between the two points is  $\delta \rho = \mathbf{x}^{pa} \cdot \tilde{\nabla} \rho$ . The limiting procedure is straightforward. First, express  $\delta \rho$  as a sum of positive and negative contributions

$$\delta \rho = \delta \rho^+ - \delta \rho^- \tag{24}$$

in which the sign convention is chosen such that  $\delta \rho^+$  and  $\delta \rho^-$  are positive

$$\delta \rho^{+} = \begin{cases} \delta \rho & \delta \rho \ge 0 \\ 0 & \delta \rho < 0 \end{cases}$$
$$\delta \rho^{-} = \begin{cases} 0 & \delta \rho \ge 0 \\ -\delta \rho & \delta \rho < 0 \end{cases}$$

For each point bordering a donor cell, we must determine  $\alpha^{\pm}$  such that

$$\rho_{\min}^a \le (\rho^a + \alpha^+ \delta \rho^+ - \alpha^- \delta \rho^-) \le \rho_{\max}^a$$

in which  $\rho^a = M/V$  is the cell average density, assumed to be the value at the centroid. The bounding factors are given by

$$\alpha^{-} \le \frac{\rho^{a} - \rho_{\min}^{a}}{\delta \rho^{-}}$$
$$\alpha^{+} \le \frac{\rho_{\max}^{a} - \rho^{a}}{\delta \rho^{+}}$$

and the limitation imposed by point p is

$$\alpha_p \le \max[0, \min(1, \alpha^-, \alpha^+)]$$

and for the entire donor cell a

$$\alpha^{\rho} \le \min \left\{ \alpha_{p} \right\}_{p}^{a} \tag{25}$$

in which the notation indicates the minimum of all surrounding points p on the surface of donor cell a. This provides a bound on the density limiter  $\alpha^{\rho}$ . As described in the next section, there may be additional constraints.

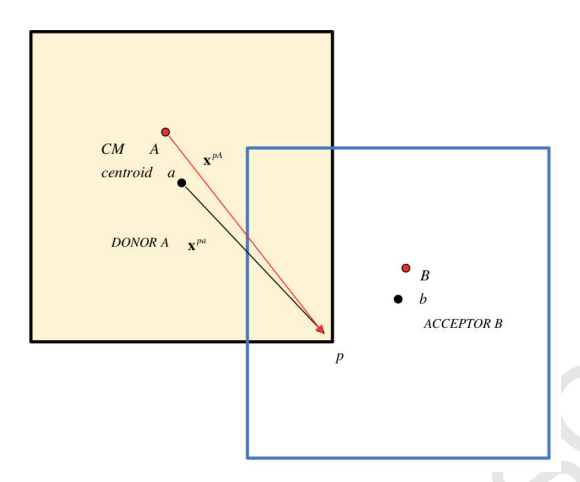


Figure 3: Projection from the centroid (a) or CM (A) to the corner of a donor cell.

Explicit limiting of internal energy density,  $\rho e$ . Although the CM reconstruction described here guarantees that  $\rho$  and specific quantities  $\phi$  are individually bounded, it does not guarantee that the product  $\rho \phi$  is bounded. In the following, we show how the product can also be limited. However, as with the Schar and Smolarkiewicz method, requiring multiple  $\phi$  fields to satisfy this can give rise to excessive dissipation. For this reason, we only require that the internal energy density  $\rho e$  be bounded. As we will show in the Sod problem of Section 6.1.1, this can make an appreciable difference. We know

$$(\rho e)_{\min} \le \rho^a e^A \le (\rho e)_{\max}$$

and must guarantee that

$$(\rho e)_{\min} \le \rho^p e^p \le (\rho e)_{\max}$$

at every node p surrounding the donor cell. The expansion for energy

$$e^p = e^A + \mathbf{x}^{pA} \cdot \tilde{\nabla} e = e^A + \delta e$$

is relative to the center of mass CM that depends upon the density gradient that is now being limited. In the following, we approximate the CM location with that obtained from the limiting of density alone. Then

$$\rho^{p} e^{p} = (\rho^{a} + \delta \rho) (e^{A} + \delta e)$$
$$= \rho^{a} e^{A} + \rho^{a} \delta e + e^{A} \delta \rho + \delta \rho \delta e$$

Consider the left inequality

$$\begin{split} 0 & \leq \left[ \rho^a e^A - (\rho e)_{\min} \right] \\ & + \left[ \rho^a \delta e^+ + e^A \delta \rho^+ + \delta \rho^+ \delta e^+ + \delta \rho^- \delta e^- \right] \\ & - \alpha^- \left[ \rho^a \delta e^- + e^A \delta \rho^- + \delta \rho^+ \delta e^- + \delta \rho^- \delta e^+ \right] \end{split}$$

in which we have inserted a factor  $\alpha^-$  to limit the negative terms. (To avoid unnecessary notational complexity, we reuse the symbols  $\alpha^\pm$  from the preceding section, but with different meaning.) Then it follows that

$$\alpha^- \leq \frac{\rho^a e^A - (\rho e)_{\min}}{\rho^a \delta e^- + e^A \delta \rho^- + \delta \rho^+ \delta e^- + \delta \rho^- \delta e^+}$$

Similarly for the right inequality

$$\alpha^+ \leq \frac{(\rho e)_{\max} - \rho^a e^A}{\rho^a \delta e^+ + e^A \delta \rho^+ + \delta \rho^+ \delta e^+ + \delta \rho^- \delta e^-}$$

Then the constraints on density and internal energy from this cell corner must be

$$\alpha^{\rho} \leq \left\{ \begin{array}{ll} \alpha^{+} & \delta \rho \geq 0 \\ \alpha^{-} & \delta \rho < 0 \end{array} \right.$$
 
$$\alpha^{e} \leq \left\{ \begin{array}{ll} \alpha^{+} & \delta e \geq 0 \\ \alpha^{-} & \delta e < 0 \end{array} \right.$$
 
$$\alpha^{\rho}, \alpha^{e} \leq \left\{ \begin{array}{ll} \sqrt{\alpha^{+}} & \delta \rho \delta e \geq 0 \\ \sqrt{\alpha^{-}} & \delta \rho \delta e < 0 \end{array} \right.$$

The square root in the last equation occurs because the product terms  $\delta\rho\delta e$  must be limited by  $\alpha$ . Then it is sufficient to limit the individual factors  $\delta\rho$  and  $\delta e$  by the square root. As in (25), the bound for the cell is the minimum of the bounds calculated for the corners. The density limiter  $\alpha^{\rho}$  is then the minimum of the above and that obtained from (25), so that the limited density gradient is

$$\nabla \rho = \alpha^{\rho} \bar{\nabla} \rho$$

The above also provides a bound on the specific internal energy limiter  $\alpha^e$ . As described in the next section, there are additional constraints.

Center of mass. Now that the limited density gradient is known, the CM of the donor cell  $(\mathbf{x}^A)$  can be calculated. This requires nonlinear polynomial integration. As shown in Appendix A, third order is needed in XY geometry and fourth order in RZ. The necessary moment integrals are derived in Appendix B.

#### 3.2. Other scalars

Other volume weighted quantities are limited as was mass density above. Specific or mass-weighted variables can be limited after the CM is determined as described above. This is done in a similar manner as density, but using the distance from the CM.

$$\mathbf{x}^{pA} = \mathbf{x}^p - \mathbf{x}^A$$
$$\delta \phi = \mathbf{x}^{pA} \cdot \tilde{\nabla} \phi$$

We must find  $\alpha^{\phi}$  such that

$$\phi_{\min}^{A} \le (\phi^{A} + \alpha^{\phi} \delta \phi) \le \phi_{\max}^{A}$$

in which  $\phi^A$  is the mass average assumed to be the value at the CM. The resulting limited gradient is

$$\nabla \phi = \alpha^{\phi} \bar{\nabla} \phi$$

In particular, this yields an additional bound on the internal energy limiter  $\alpha^e$  that becomes the minimum of the new bound and that from the preceding section. The limited internal energy gradient is then

$$\nabla e = \alpha^e \bar{\nabla} e$$

#### 3.3. Vectors and tensors

Monotonicity is basically a scalar notion that does not extend directly to vectors and tensors. We require that vector and tensor variables be bounded in a non-directional manner. Here, we describe three methods for accomplishing this and test them in Section 6.

Component limiting. A common method of limiting both vector and tensor gradients is to simply treat each component in the global coordinate system as a scalar, creating a limiting coefficient for each. This approach is known to produce asymmetry in radial flow problems that can be reduced by applying the smallest coefficient to all components. However, a consequence is that minor perturbations in one direction can limit gradients in other directions.

Tensor limiting. If, instead of a global coordinate system, the components of a vector are limited in a physically relevant one, the notion of component limiting can be significantly improved. Maire [57] proposed a limiter calculated in the principal coordinate system of the unlimited velocity gradient. We have previously used this in a Lagrangian context [16, 19], and here apply it to the remap problem. In the global system, the unlimited extrapolation to each bounding point from the CM of a cell is

$$\delta \mathbf{u} = (\mathbf{x}^p - \mathbf{x}^A) \cdot \tilde{\nabla} \mathbf{u}$$

We wish to limit the gradient with a tensor L so that

$$\mathbf{u}^p = \mathbf{u}^A + \mathbf{L} \cdot \delta \mathbf{u}$$

The eigenvectors of the velocity gradient tensor are used to construct a rotation matrix  $\mathbf{R}$  in each cell. We denote vectors in the rotated system with a bar so that  $\mathbf{\bar{u}} = \mathbf{R}\mathbf{u}$  and

$$\bar{\mathbf{u}}^p = \bar{\mathbf{u}}^A + \bar{\mathbf{L}} \cdot \delta \bar{\mathbf{u}}$$

In the rotated system,  $\bar{\mathbf{L}}$  is a diagonal tensor whose components are the coefficients determined from component limiting in this system. A complication is that the bounds for velocity components in each cell must be determined by rotating velocities in adjacent cells to the same coordinate system. Given  $\bar{\mathbf{L}}$ , the tensor in the global system is then

$$\mathbf{L} = \mathbf{R}^{-1} \mathbf{\bar{L}} \mathbf{R}$$

so that the limited velocity gradient becomes

$$\nabla \mathbf{n} - \mathbf{I} \cdot \tilde{\nabla} \mathbf{n}$$

To our knowledge, the tensor limiter method has not been previously applied to the stress gradient because the proper coordinate system for the gradient of a tensor is less obvious. Here, we choose such a system by requiring that force density, instead of the stress tensor itself, be bounded. The force density is the projection of the stress tensor in the direction of acceleration (stress divergence)

$$\mathbf{f} = \boldsymbol{\sigma} \cdot \hat{\mathbf{n}}$$

in which the unit vector is

$$\hat{\mathbf{n}} = \frac{\tilde{\nabla} \cdot \boldsymbol{\sigma}}{\left| \tilde{\nabla} \cdot \boldsymbol{\sigma} \right|}$$

The solution is now analogous to that for velocity. Eigenvectors of  $\tilde{\nabla} f$  are used to construct a rotation matrix and limiting coefficients are calculated in the rotated frame

$$\mathbf{\bar{f}}^p = \mathbf{\bar{f}}^a + \mathbf{\bar{L}} \cdot \delta \mathbf{\bar{f}}$$

in which the centroid is used for the extrapolation instead of the CM because stress is a volume weighted field. Again, the forces in adjacent cells must also be rotated to determine the bounds. After rotation back to the global frame, the limited stress gradient is given by

$$\nabla \sigma = \mathbf{L} \cdot \tilde{\nabla} \sigma$$

Limiting of rotational invariants. A third strategy is based upon limiting of rotational invariants, so that velocity and stress can be limited independently of orientation. In a Lagrangian context, we used this method to limit the stress tensor in [16, 69]. The method has a conceptual issue in that, by design, it is insensitive to variations in orientation.

For velocity, the rotational invariant is the specific kinetic energy. From the Lagrange step, we know that (Section 2.2), the compatible kinetic energy has a linear, not quadratic distribution. Thus, if velocity is reconstructed linearly  $\tilde{\nabla} \mathbf{u}$ , the gradient of the linearized kinetic energy is

$$\tilde{\nabla}k = (\tilde{\nabla}\mathbf{u}) \cdot \mathbf{u}^A$$

in which  $\mathbf{u}^A$  is the velocity at the CM of the donor cell. The kinetic energy can then be limited as other specific fields yielding  $\alpha^k$ . The limiter for the velocity is the same as the limiter for the linearized kinetic energy  $\alpha^u = \alpha^k$ .

In practice, this velocity limiter has limited utility because it is not Galilean invariant. However, a similar strategy applied to the deviatoric stress tensor  $\mathbf{s}$  is useful, as we described in [16, 69]. The stress tensor is decomposed into mean  $\pi$  and deviatoric  $\mathbf{s}$  stress components

$$\sigma = \mathbf{1}\pi + \mathbf{s}$$

in which  $\pi = tr(\sigma)/3$ . The deviatoric stress has a rotational invariant

$$y = \mathbf{s} : \mathbf{s}/2 \tag{26}$$

The linearized gradient of the second deviatoric invariant  $y = \mathbf{s} : \mathbf{s}/2$ , is given by

$$\tilde{\nabla} y = (\tilde{\nabla} \mathbf{s}) : \mathbf{s}^a$$

in which  $\mathbf{s}^a$  is the deviatoric stress at the centroid and  $\tilde{\nabla}\mathbf{s}$  is the unlimited gradient. The quantity y can then be limited as was mass density, yielding  $\alpha^y$ . Because the gradients of the deviatoric stress tensor and the second invariant are related, the limiter for the deviatoric tensor is the same as that of the invariant  $\alpha^s = \alpha^y$ .

#### 4. Conservative remap

Having addressed the Lagrange and reconstruction steps, we now turn to a new conservative remap method for polynomial distributions. With respect to the GCL, we note that volume compatibility is satisfied exactly in Cartesian geometry by the exact intersection methodology. In axisymmetric geometry, it is also satisfied exactly but requires the polynomial integrals of Appendix A.

For the distributions of  $\rho$  and  $\phi$  of (23), the product  $\rho(\mathbf{x})\phi(\mathbf{x})$  is a higher than second order polynomial. In Appendix B, we consider general volume integrals of such polynomials. However, referring to (21), the integrals *for linear functions in the CM formulation* reduce to simply mass times the value of the reconstruction  $\phi(\mathbf{x}^{\mathbf{I}})$  at the CM of the volume of intersection

$$\Phi^{I} = \int_{I} dV \rho(\mathbf{x}) \phi(\mathbf{x})$$
$$= M^{I} \phi^{I}$$

in which  $\phi^{I}$  is the value of  $\phi(\mathbf{x})$  at the CM of the intersection volume.

As was the case for the donor cell A, determining the location of the CM ( $\mathbf{x}^I$ ) requires nonlinear polynomial integration. As shown in Appendix A, third order is needed in XY geometry and fourth order in RZ. Again, the necessary moment integrals are derived in Appendix B.

#### 4.1. Remap

We consider first the generalized densities  $\{\rho, \sigma\}$ . As illustrated in Figure 4, given the donor cell centroid  $\mathbf{x}^a$ , the distance to the intersection volume centroid  $\mathbf{x}^i$  is

$$\mathbf{x}^{ia} = \mathbf{x}^i - \mathbf{x}^a$$

Using the limited gradients from Section 3.1, the value of the mass density at the intersection centroid is

$$\rho\left(\mathbf{x}^{i}\right) = \rho^{a} + \mathbf{x}^{ia} \cdot \nabla \rho$$

and the mass is

$$M^{I} = V^{I} \rho \left( \mathbf{x}^{i} \right)$$

This is accumulated into the acceptor cell B

$$M^B = \sum_{I}^{B} M^I$$

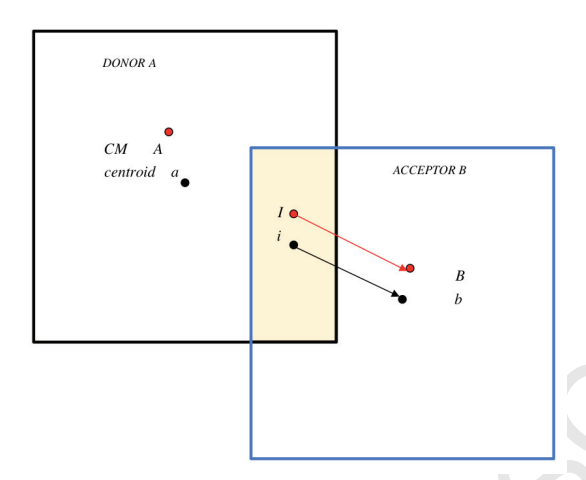


Figure 4: Illustration of conservative remap from an intersection volume I to an acceptor cell B.

so that the final remapped density is

$$\rho^B = M^B/V^B$$

The remaining generalized densities are remapped similarly.

The corresponding equations for remapping specific quantities  $\{\mathbf{u}, k, e\}$  are also similar. The distance from the cell CM  $\mathbf{x}^A$  to the intersection CM  $\mathbf{x}^I$  is

 $\mathbf{x}^{IA} = \mathbf{x}^I - \mathbf{x}^A$ 

For specific variables, the set of remap equations is

$$\phi(\mathbf{x}^{I}) = \phi^{A} + \mathbf{x}^{iA} \cdot \nabla \phi$$

$$\mathbf{\Phi}^{I} = M^{I} \phi(\mathbf{x}^{I})$$

$$\mathbf{\Phi}^{B} = \sum_{I}^{B} \mathbf{\Phi}^{I}$$

$$\phi^{B} = \mathbf{\Phi}^{B} / M^{B}$$

again with the other specific primitives remapped in the same way.

#### 5. Entropy production

We now turn to the remaining repartition or entropy production step. Our new method for calculating dissipation (entropy production) in remap bears some similarity with KE fixup described in Section 1. However, we question the underlying principle that the cell kinetic energy must be compatible with the cell momentum,  $U^2/2M$ . For later reference, we define specific quantities

$$q = Q/M$$
$$\mathbf{u} = \mathbf{U}/M$$
$$e = E/M$$

As only the acceptor cell is involved in this section, we will omit the superscript B on variables.

In the remap, internal energy E and kinetic energy K from the Lagrange step are first remapped conservatively and isentropically; that is, they are individually conserved without energy exchange between the two components. A

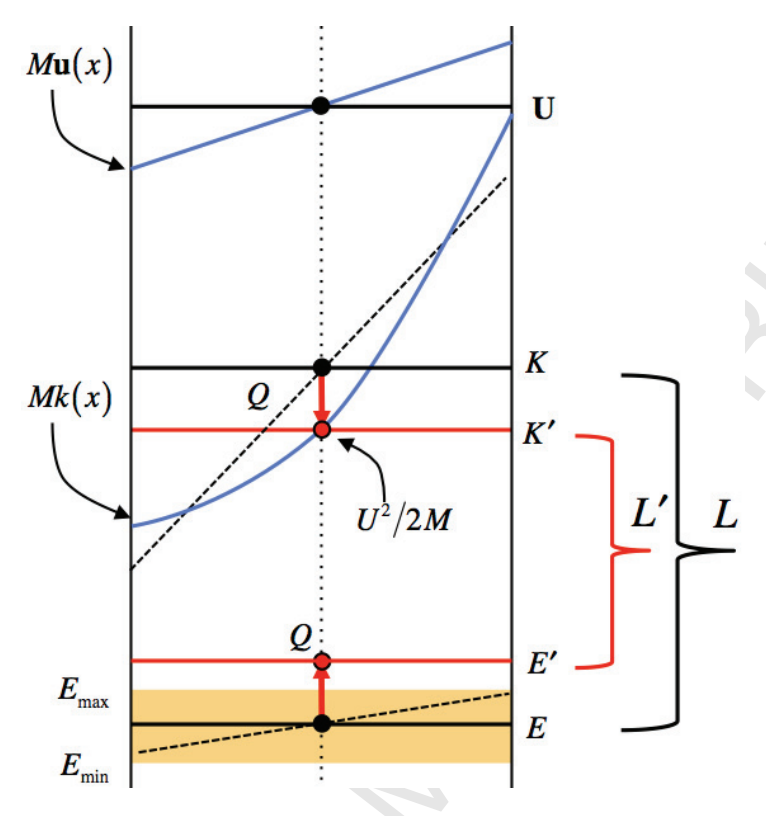


Figure 5: Kinetic and internal energy are first remapped isentropically. Then dissipation is introduced to enforce consistency between the cell averaged momentum and kinetic energy. A linear velocity distribution and the corresponding quadratic kinetic energy distributions are shown in blue. The midpoint of the kinetic energy distribution (a red dot) corresponds to the cell average velocity. Conserved quantities are represented by horizontal black lines, and the repartitioned energies in red. The internal energy bounds are represented as a shaded region.

typical situation is illustrated in Figure 5 that depicts a distribution of the relevant quantities across the acceptor cell. A linear velocity distribution and the corresponding quadratic kinetic energy distributions are shown in blue. The midpoint of the kinetic energy distribution (a red dot) corresponds to the cell average velocity. Conserved quantities are represented by horizontal black lines, and the repartitioned energies in red. The internal energy bounds are represented as an orange shaded region.

For a simple system, the underlying physical principle in the repartition is analogous to a *Least Action* notion that minimizes the Lagrangian functional in the cell

$$L = K - E$$

subject to constraints. To do this, dissipation is introduced by conservatively transferring kinetic to internal energy

$$K' = K - Q \tag{27}$$

$$E' = E + Q \tag{28}$$

$$H' = H \tag{29}$$

so that  $total\ energy$  is always conserved independent of the definition of Q. After the transfer, the resulting Lagrangian is smaller

$$L'=K'+E'=L-2Q$$

There are constraints on Q. We consider two alternatives.

Canonical dissipation method. In the canonical dissipation method, the dissipation is always taken to be

$$Q = K - \mathbf{U}^2 / 2M$$

so that the cell kinetic energy is forced to be consistent with the cell momentum

$$K' = \mathbf{U}^2 / 2M$$

In Figure 5, this drops the kinetic energy from the black line K to the red line K' and increases the internal energy from the black line E to the red line E'. This can move the internal energy outside the bounds denoted by the orange region. As we show in Section 6.2.2, this leads to overheating in flows such as isentropic compressions.

Compatible dissipation method. The compatible dissipation method further asserts that the dissipation must not force the internal energy out of equilibrium with the surroundings. That is, Q must be constrained such that

$$e_{\min} \le e' \le e_{\max}$$

Because this is an *a posteriori* calculation, bounds are determined from all donor cells that contribute to each acceptor cell. With Q defined as above, the necessary limiter is given by

$$\alpha = \min\left(1, \ \frac{M}{Q^{-}}\left(e - e_{\min}\right), \ \frac{M}{Q^{+}}\left(e_{\max} - e\right)\right)$$

in which  $Q = Q^+ - Q^-$  has been decomposed for limiting as was density. As before, superscripts + and - denote positive and negative contributions. Then Q is replaced by  $\alpha Q$ , and the conserved energies are again as in (27). We temporarily defer discussion of the implications of negative Q.

If Q does not need to be limited, the result is the same as in the canonical method. In general, however,  $K' \neq U^2/2M$ . The algorithmic implication is that the cell kinetic energy must be time integrated, as opposed to being inferred from the cell average velocity. This is as described in the rate based partitioning of the Lagrange step of Section 2.

State at the integration point. Recall that partitioning of energy in the Lagrange step and the repartitioning after the remap is done solely to obtain specific internal energy at an integration point  $\mathbf{x}$ . This is then used in the constitutive model to evaluate stress. The state at the integration point is given by

$$k'(\mathbf{x}) = \frac{1}{2}\mathbf{u}^{2}(\mathbf{x})$$

$$e'(\mathbf{x}) = e + q$$

$$h'(\mathbf{x}) = k'(\mathbf{x}) + e'(\mathbf{x})$$

so that the *specific kinetic energy at the point is always compatible with the velocity at that point.* However, neither kinetic nor total energy at the integration point necessarily equal the cell average.

$$k' \neq K'/M$$
  
 $h' \neq H'/M$ 

*Positivity of Q.* Recall that K and E are remapped isentropically, so that Q represents a change in entropy. The Second Law requires that it be positive, and positivity is supported by the Cauchy-Schwartz inequality. Consider a fluid volume with fields  $\rho$  and  $\mathbf{u}$  distributed in an arbitrary manner. The total mass, momentum, and kinetic energy is

given by

$$M = \int \rho dV$$

$$\mathbf{U} = \int \rho \mathbf{u} dV$$

$$K = \int \frac{1}{2} \rho \mathbf{u}^2 dV$$

Applying the integral form of the Cauchy-Schwartz inequality yields

$$\left\{ \int \rho \mathbf{u} dV \right\}^2 \leq \left\{ \int \rho dV \right\} \left\{ \int \rho \mathbf{u}^2 dV \right\}$$

or

$$U^2 < 2MK$$

Then

$$Q = K - \frac{\mathbf{U}^2}{2M} \ge 0$$

To this point, we find that our dissipation formulation allows Q to be negative. The explanation is that the conditions of the Cauchy-Schwartz inequality are not exactly met. The inequality requires compatibility between the momentum  $\rho \mathbf{u}$  and kinetic energy  $\frac{1}{2}\rho \mathbf{u}^2$  at every point in space, thereby requiring a quadratic form for the latter. Yet, we remap both velocity and kinetic energy with linear reconstructions.

In a separate unreported study, we did remap kinetic energy as a quadratic function, and found that indeed Q was always positive. This approach was not followed here because it would require substantial changes in the underlying Lagrange method, contradicting our design goal. The incompatibility in the two assumed velocity distributions in the CCH Lagrange formulation was described in Section 2.2. That is, the Lagrange partitioning of total energy corresponds to a linear, not quadratic, distribution of kinetic energy. If one were to remap kinetic energy as a quadratic function, the cell kinetic energy would increase relative to the Lagrange partitioning. Conservation would then require the change to be subtracted from the cell internal energy. As this happens to varying degrees in all cells, there appears to be no obvious way to establish bounds for the reduced internal energy.

Although the dissipation formulation does not guarantee that Q is positive, we constrain it to be so

$$Q \ge 0$$

This has no effect on conservation. There appear to be no detrimental consequences, as we have also run most test problems with and without the constraint and found insignificant differences. Section 6.1.3 explores this issue in the case of the Sedov problem.

#### 6. Test problems

Our fundamental objective is to find remap methods that produce excellent results over a wide range of situations. To this end, we consider test problems with and without shocks, high and low speed flow, with and without vorticity, gases and solids, and rectangular and polar grids. All test problems were in XY geometry and involved single materials. To stress the numerical methods, relatively coarse meshes were used. Most problems were run in an Eulerian mode in which the remap is back to the original mesh, but a few were run in an ALE mode using mesh relaxation based on a Laplacian smoothing method [38], the details of which are beyond the scope of this paper. The underlying Lagrangian hydro method was the cell-centered CGR scheme from [19] and described in Section 2. Flux volumes were calculated using an exact intersection method that made no assumptions about similar connectivity between the

donor and acceptor meshes [20, 17, 18, 43]. The test problems do not specifically test the capability of the formulation to remap between meshes of the same or differing connectivity, but this was done in [22, 21] for two ReALE problems. There were three principal areas of comparison in the test problems:

- 1. CM vs. CV reconstruction. The CM formulation is as previously described in Sections 3 and 4 in which density  $\rho$  and specific variables  $\phi$  are separately limited. In CV methods, the conserved products  $\rho\phi$  are bounded, but as discussed in Section 1, the specific fields are not necessarily bounded. As noted in the Introduction, the CV method has a number of known limitations for which a variety of extensions have been proposed. We made no attempt to assess these extensions to CV, but rather offered an alternative scheme (CM) that does not have the deficiencies.
- 2. CE, IE, TE energy modes. The internal energy (IE) method remaps only internal energy and has no entropy production mechanism. The compatible energy (CE) and the total energy (TE) methods were as described in Section 5. In contrast to IE, both CE and TE create entropy as a consequence of the remap. In the CE method, the specific kinetic energy at the cell center is compatible with the velocity at that location.
- 3. Limiters. For both the velocity and stress gradients, comparisons are made between the tensor, component, and rotationally invariant methods described in Section 3.3. For CM reconstruction, the effect of an additional limiter for the product  $\rho e$  (Section 3.1) is also considered.

This gave rise to five algorithmic configurations that were the focus of the testing: CM-CE, CM-IE, CM-TE, CV-IE, and CV-TE. Ultimately, the CM-CE configuration was found to yield the best results and was designated as the *baseline* method in the comparisons. In addition, a few comparisons are also made between alternative methods for limiting velocity and stress.

#### 6.1. Shock-dominated problems

The three shock problems use polytropic gases. In the *Sod* problem, a shock forms at a contact discontinuity. In the *Noh* problem, the shock forms as a reflection from the origin due to a radially inward initial flow. The problem involves both high and low speed flow. The shock in the *Sedov* problem is produced by a high energy source at the origin.

### 6.1.1. Sod shock tube

The Sod shock tube is a very well known problem defined in [73]. It consists of a shock tube of 100 units in length. The interface is located at x = 50. At the initial time, the states on the left and the right sides of the interface are uniform. The left state is a high pressure fluid characterized by  $\{\rho_L, p_L, u_L\} = \{1, 1, 0\}$  the right state is a low pressure fluid defined by  $\{\rho_R, p_R, u_R\} = \{0.125, 0.1, 0\}$ . The fluid is a polytropic gas defined by  $\gamma = 7/5$ . Physically, the problem is 1D, but we modeled it on a 2D mesh. The computational domain is defined by  $[x, y] \in [0, 100] \times [0, 10]$ . The initial mesh is a Cartesian grid with  $100 \times 2$  cells. The boundary conditions are reflective. The problem was run in an Eulerian mode.

CV reconstruction. In Figure 6, we compare the CV reconstruction method in internal and total energy modes (CV-IE and CV-TE) with our baseline method CM-CE. The CV-IE result is low because energy is not conserved, while the CV-TE displays an overshoot at the contact discontinuity because monotonicity of specific internal energy is not guaranteed by the CV method.

*CM reconstruction.* Figure 7(a) compares the CM method in CE, IE and TE modes. The CE and TE results are essentially identical, while the IE result is low, again because energy is not conserved. In Figure 7(b), we compare the CM-CE method with (red) and without (green) the explicit limiting of internal energy density  $\rho e$  discussed in Section 3.1. The overshoot is significantly reduced with the additional limiting.

### 6.1.2. Noh problem

The Noh problem [63] has been used extensively to illustrate the difficulties of preserving symmetry as well as exposing tendencies to produce a well known entropy error known as wall heating [24]. The material is a polytropic gas with  $\gamma = 5/3$ . Initially the velocity is directed radially inward with a unity magnitude, the density is unity, and

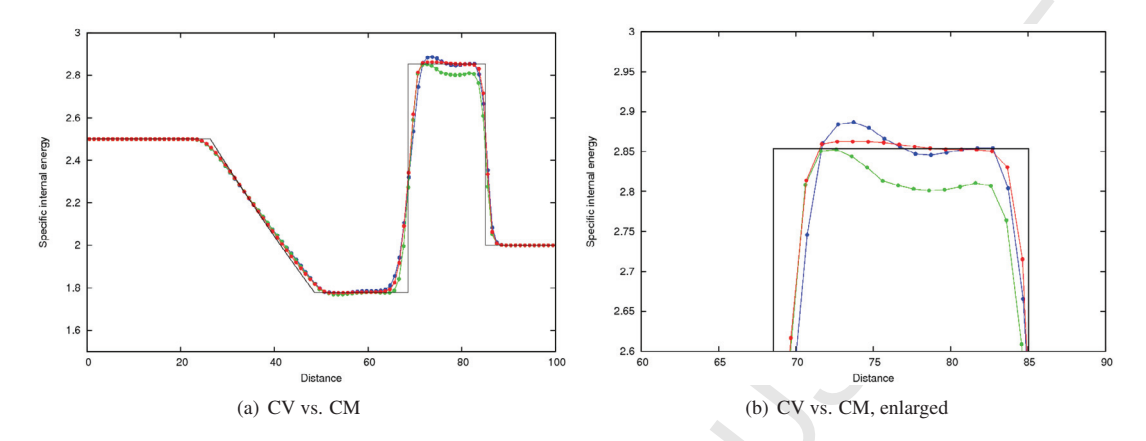


Figure 6: Sod: Specific internal energy vs. distance at t=1.0. The baseline CM-CE reconstruction method (red) is compared with the CV-IE (green) and CV-TE (blue) methods. The analytical solution is black. The CV-IE result is low because energy is not conserved, while the CV-TE displays an overshoot at the contact discontinuity.

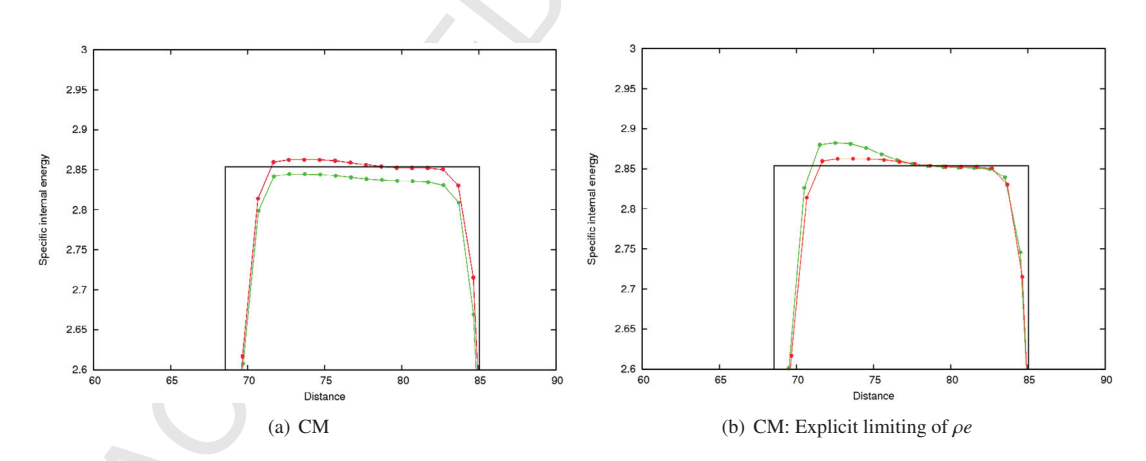


Figure 7: Sod, CM reconstruction method: specific internal energy vs. distance at t=1.0. In (a) we compare the CE, IE and TE modes. The analytical solution is black. The CE and TE results (red) are identical, while the IE result (green) is low. In (b) we compare CM-CE reconstruction with (red) and without (green) the explicit limiting of internal energy density  $\rho e$  described in Section 3.1. The overshoot is significantly reduced with the additional limiting.

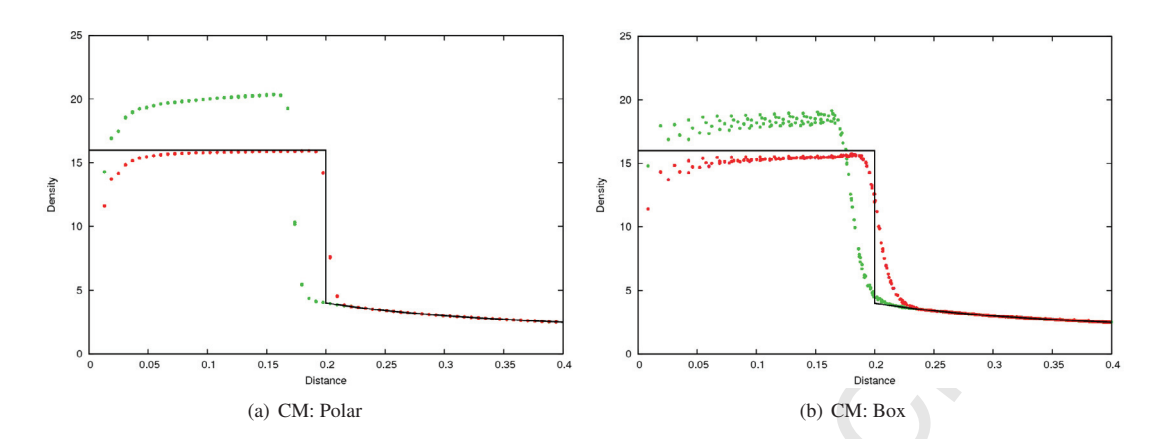


Figure 8: Noh, CM reconstruction method: scatter plot of density vs. distance at t=0.6 on polar (a) and box (b) meshes. We compare the CE/TE (red) and IE energy modes (green). The CE and TE modes agree well with the analytical result (black), but the IE result has a slow propagation velocity and misses the shock state.

the internal energy is small  $(10^{-4})$ . The converging flow causes a shock to form at the origin and propagate radially outward. The density plateau behind the shock wave reaches a uniform value of 16 in XY and 64 in RZ out to a radius of 0.2 at t=0.6. Numerically, the proper density near the origin is not obtained because of the aforementioned wall heating.

Here, we consider the Noh problem in XY geometry on both a  $10 \times 200$  polar mesh and a  $100 \times 100$  rectangular mesh. Outer boundaries were at a distance of 1.2 from the origin. Boundary conditions were reflecting along the axes and fixed at the outer surfaces. The fixed outer boundary causes a perturbation that propagates inward, so that the solution must be evaluated in window near the origin. The problems were run in an Eulerian mode to maximize the amount of remap.

*CM reconstruction.* In Figures 8(a) and (b), we compare the CM reconstruction method for energy modes CE/TE (red) and IE (green). For both types of meshes, the CE and TE results are identical because both methods conserve total energy. They agree well with the analytic solution (black), while the CV-IE result has a slow propagation velocity and misses the shock state. This is a result of insufficient entropy production and lack of energy conservation (a loss of about 6 percent on the polar mesh and 3 percent on the box mesh).

CV reconstruction. In Figures 9(a) and (b), we compare the baseline method CM-CE (red) with the CV reconstruction method in internal and total energy modes (CV-IE and CV-TE) in green and blue respectively. Aside from the well-known wall heating at the origin, the CM result agrees well with the analytic solution (black). Again, the CV-IE result has a slow propagation velocity, misses the shock state, and has an energy loss of about 3 percent on the polar mesh and 5 percent on the box mesh. Although the CV-TE result has about the correct average amplitude and position, it is clearly unstable on both meshes because monotonicity of specific internal energy is not guaranteed by the CV method.

*Velocity limiter.* In Figure 10, for the baseline CM-CE method, we compare the tensor velocity limiter (red) of Section 3.3 with a simple component limiter (green) and the rotationally invariant limiter (blue). The tensor and component limiters produce nearly identical results, whereas the invariant limiter results are scattered.

#### 6.1.3. Sedov blast wave

In this section, we present results of the Sedov blast wave [71] as an example of a diverging shock wave with a similarity solution. The initial setup consists of a square grid extending from 0 to 1.2 in both x and y directions defining a single quadrant. Calculations were run in XY geometry on a  $200 \times 200$  square mesh in an Eulerian mode. All boundaries are reflective. The material is a polytropic gas with  $\gamma=1.4$ , initial density of unity, and initial velocity zero everywhere. The specific internal energy is effectively zero ( $10^{-6}$ ) except in the source region that is modeled using a finite volume source at the origin [65]. The source region was  $0.024 \times 0.024$  with a specific internal energy of 426.943.

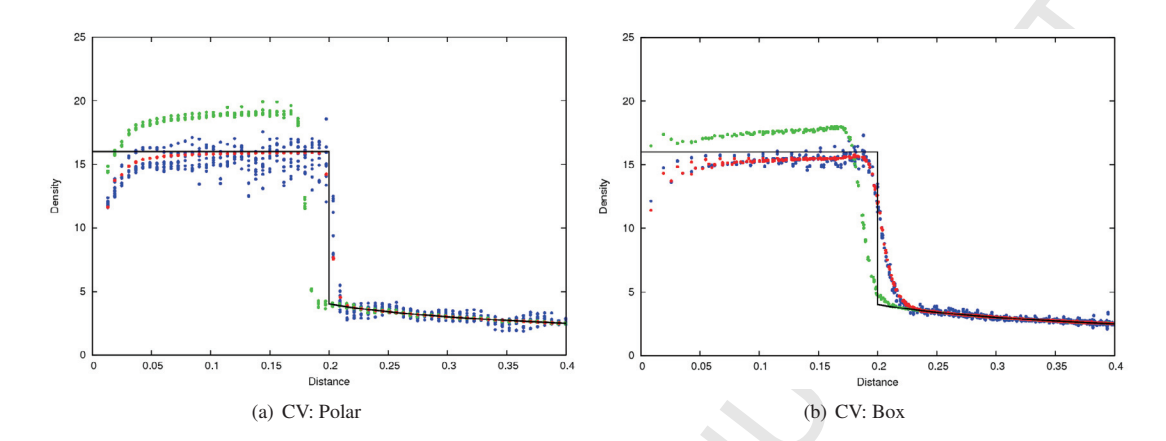


Figure 9: Noh, CV reconstruction method: scatter plot of density at t=0.6 on polar (a) and box (b) meshes. We compare the baseline CM-CE reconstruction method (red) with the CV-IE (green) and CV-TE (blue) methods. The CV-IE result has a slow propagation velocity and misses the shock state, while the CV-TE is unstable on both meshes.

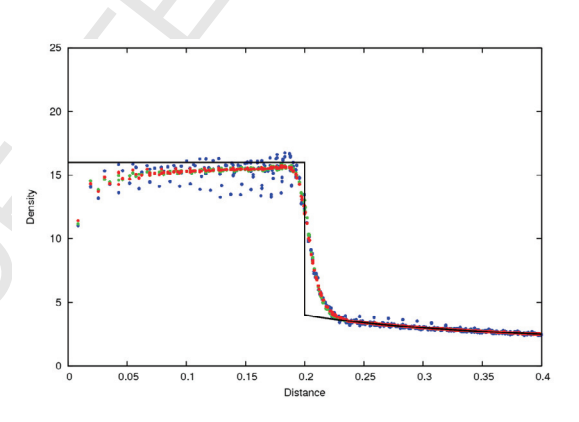


Figure 10: Noh, CM-CE baseline: scatter plot of density at t=0.6 on a box (b) mesh, comparing the tensor (red), component (green), and rotationally invariant (blue) velocity limiters. The rotationally invariant limiter performs poorly.

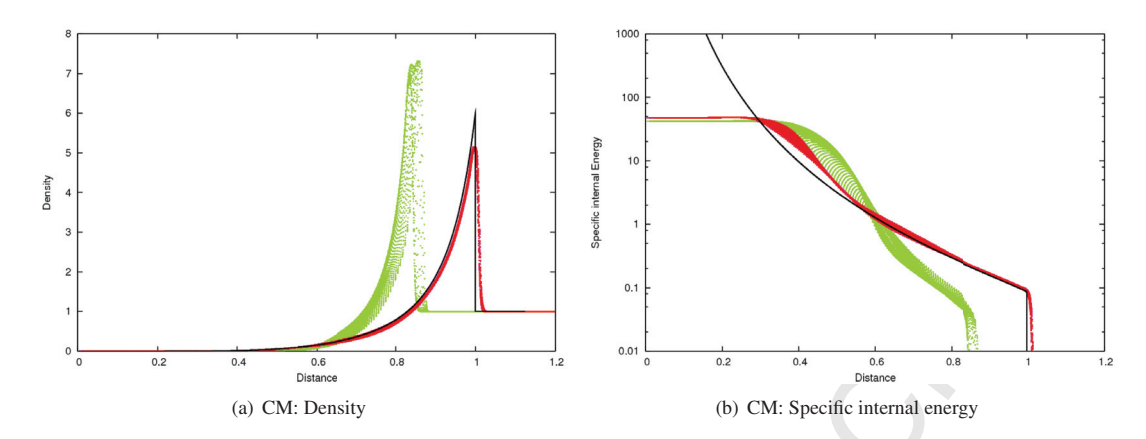


Figure 11: Sedov, CM reconstruction: scatter plots of density (a) and specific internal energy (b) vs. distance at t=1.0. We compare the CE/TE (red) and IE energy modes (green). The CE and TE modes are nearly identical and agree well with the analytical result (black), but the IE result had a slow propagation velocity and missed the shock state in both density and energy.

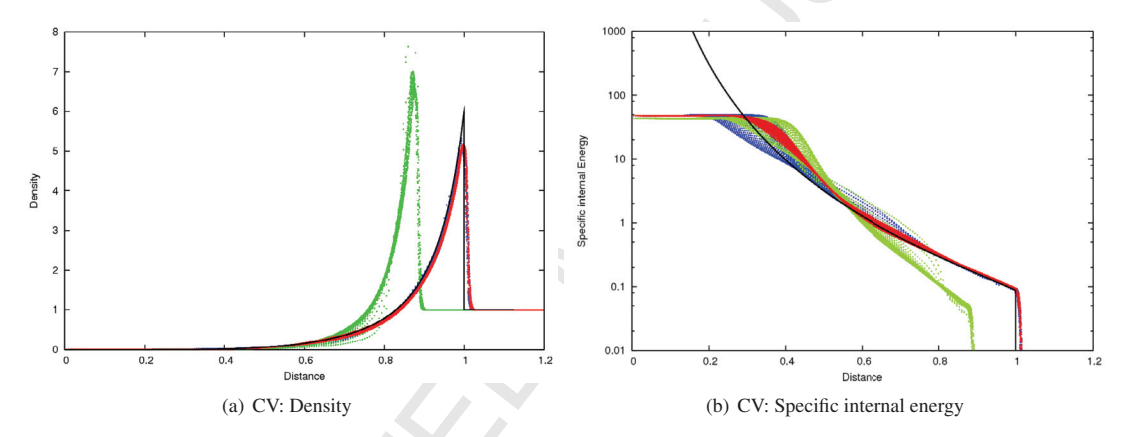


Figure 12: Sedov, CV reconstruction: scatter plots of density (a) and specific internal energy (b) vs. distance at t=1.0. We compare the baseline CM-CE reconstruction method (red) with the CV-IE (green) and CV-TE (blue) methods. The CM-CE and CV-TE results are similar, but the CV-IE result is substantially in error.

*CM reconstruction.* Figure 11(a) is a scatter plot of density vs. distance, and (b) is the specific internal energy on a logarithmic scale. We compare the CM reconstruction method for energy modes CE/TE (red) and IE (green). As was the case for the Noh problem of Section 6.1.2, the CE/TE results are identical because both methods conserve total energy, and both agree well with the analytic solution (black). The IE result had a slow propagation velocity and had energy errors spanning two orders of magnitude. Again, the poor IE result is a consequence of insufficient entropy production and lack of energy conservation.

CV reconstruction. In Figure 12, we compare the baseline CM-CE reconstruction method (red) with the CV-IE (green) and CV-TE (blue) methods. With regard to density, the CM-CE and CV-TE results are nearly identical, but some differences appear in the specific internal energy. Again, the CV-IE results are in error by a substantial amount.

Sign of Q. The quantity Q of Section 5 is not an artificial viscosity, but is related to dissipation and has units of energy. As discussed in Section 5, Q can be negative unless explicitly constrained to be positive. Here, we remove this constraint in a Sedov calculation to evaluate the magnitude of the negativity. Recall that Q is extensive and that the specific quantity is

$$q = Q/M$$

Figure 13 shows regions of positive q in (a) and negative in (b). It is essentially zero except at the shock position

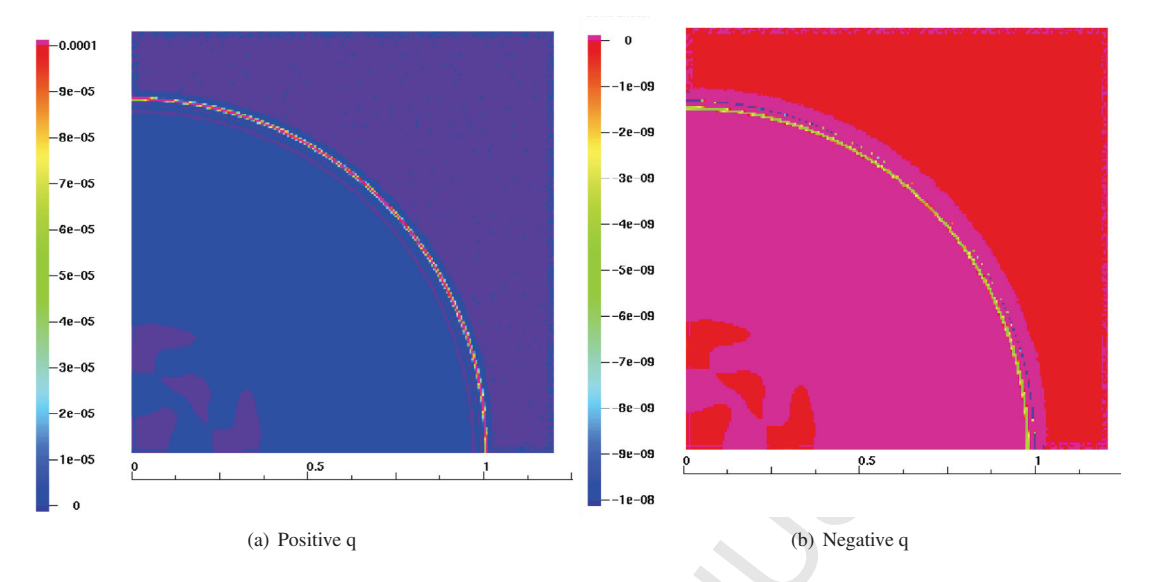


Figure 13: Sedov, CM-CE method: Regions of positive (a) and negative (b) q clearly delineate the shock position. Regions of q nearly zero are shaded blue or dark purple in (a) and red or light purple in (b). Recall that q = Q/M.

where it has a maximum of about  $10^{-4}$ . Regions of negative q have magnitudes as large as  $10^{-8}$  near the shock, four orders of magnitude lower than the adjacent positive values. In Figure 13, regions of q nearly zero are shaded blue or dark purple in (a) and red or light purple in (b). Although the test problems presented in this article had q constrained to be positive, we have also run most without the constraint and found insignificant differences.

#### 6.2. Smooth and adiabatic flow problems

The first three problems involve adiabatic flow. In the *Adiabatic Release* problem, material is first shocked, and then the energy is tracked along the release adiabat. The *Coggeshall* problem describes adiabatic compression due to an initial velocity gradient, while the *Kidder shell* problem drives the material adiabatically with a time-dependent pressure boundary condition. The *Taylor-Green* problem represents a vortical flow for which there is a known solution. The preceding problems involve polytropic gases. The *Howell* problem involves a solid constitutive model and simulates the collapse of a Be cylinder with an initial velocity distribution.

#### 6.2.1. Adiabatic release

This test problem was originally posed by G. Bazan and R. Rieben [4] to verify the ability to follow adiabatic release down an isentrope following shock compression to Hugoniot density. An extensive code comparison was done in [64].

The problem can be viewed as a 1D Riemann problem split into two materials with a contact discontinuity at x=0.3 as shown in Figure 14. Each material is defined with the following equation of state

$$p(\rho) = \left(\frac{\rho}{\rho_0} - 1\right)\rho_0 c_0^2 \tag{30}$$

in which  $\rho_0$  is the initial density,  $\rho$  is density, and the sound speed at reference density is  $c_0 = 0.4$ . The initial conditions are

$$\{u, \rho, e\}_L = \{0.5, 16, 0\}$$

$$\{u, \rho, e\}_R = \{0.0, 16, 0\}$$
(31)

The boundary conditions at each end are free, so that the problem was run in an ALE mode. As specified, the diagnostics consist of two Lagrangian tracer particles located initially at x = 0.36 and x = 0.84, but we only follow



Figure 14: Adiabatic release. Initial configuration.

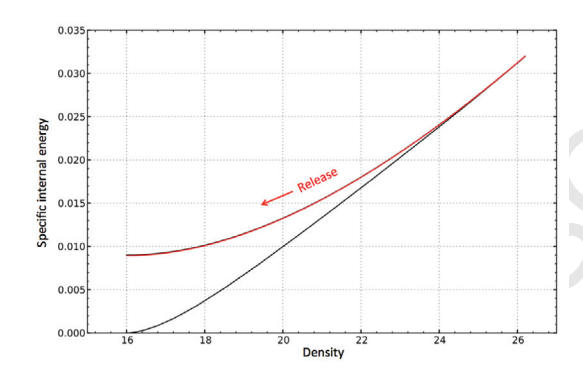


Figure 15: Adiabatic release: specific internal energy vs. density during loading and release along the adiabat.

the second here. The calculational mesh was 2x360 on a domain  $x \in [0.005, 0.9]$  so that the cell size was 0.0025 in both x and y directions.

The problem is run until t = 1.4 by which time a shock has formed at the contact, interacted with the second tracer at about  $t \sim 0.83$ , formed a rarefaction at the free surface, and begun the release at the tracer location at about  $t \sim 0.98$ . As originally defined, the problem was to be run in a Lagrangian mode, so that the tracer moved with the material. In our ALE simulation, the tracer is stationary.

An expression for the specific internal energy along the adiabat is easily derived. Following [4, 64]

$$u_p = \frac{1}{2}u_L \tag{32}$$

Based upon the initial conditions, the Hugoniot values are

$$p_{H} = \rho_{0}u_{p}\left(c_{0} + u_{p}\right)$$

$$\rho_{H} = \rho_{0}\left(1 + \frac{u_{p}}{c_{0}}\right)$$

$$e_{H} = \frac{p_{H}\rho_{H} - \rho_{0}}{2\rho_{H}\rho_{0}}$$
(33)

The adiabatic energy as a function of density is given by

$$e_A(\rho) = e_H + c_0^2 \left[ \frac{\rho - \rho_H}{\rho_0} - \ln \left( \frac{\rho}{\rho_H} \right) \right]$$
 (34)

The figure of merit is the percentage error in this quantity. The specific internal energy as a function of density during loading and release is shown in Figure 15.

*CM reconstruction.* Figures 16(a) and (b) show the log of the error in specific internal energy along the adiabat as a function of density. Figure 16(a) compares energy modes for CM reconstruction. CM-CE (red) and CM-TE (not shown) are coincident, while CM-IE was in error by about 10 percent. The CM-CE result had an error of about 0.1 percent and compares very favorably with results in Reference [64].

CV reconstruction. Figure 16(b) compares the baseline CM-CE method (red) with CV-IE (green) and CV-TE (blue). Both CV results were in error by about 10 percent.

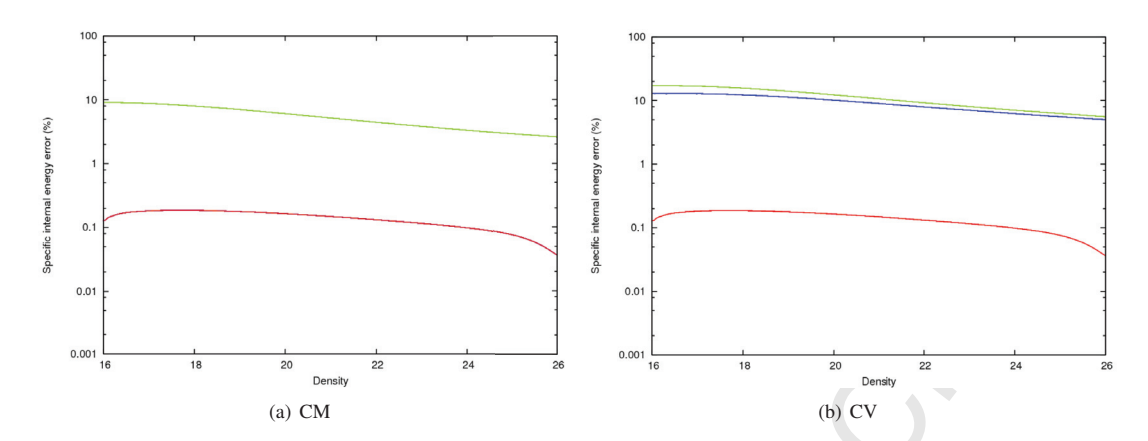


Figure 16: Adiabatic release: percent error in specific internal energy vs. density along the adiabat for 2x360 mesh. In (a) CM-CE (red) and CM-TE are coincident while CM-IE (green) has a much larger error. In (b) CM-CE (red) is compared with CV-IE (green) and CV-TE (blue) both of which had large errors.

#### 6.2.2. Coggeshall problem

The Coggeshall problem [27] describes the adiabatic compression of a polytropic gas with  $\gamma = 5/3$ . It is similar to the Noh problem of Section 6.1.2 except the initial velocity is equal to the negative of the coordinate instead of unity. The analytic solution is given by

$$u(t) = u_0$$

$$r(t) = r_0 (1 - t)$$

$$\rho(t) = \rho_0 (1 - t)^{-\alpha}$$

$$e(t) = e_0 (1 - t)^{-\alpha(\gamma - 1)}$$

in which  $\alpha = \{1, 2, 3\}$  respectively for planar, cylindrical, or spherical geometry.

We ran a 2D XY configuration in an Eulerian mode on a  $200 \times 200$  mesh and a calculational domain extending from 0 to 5 in both x and y directions. The initial conditions were  $\{u_0, \rho_0, e_0\} = \{-r_0, 1.0, 10^{-6}\}$  in which  $r_0$  is the initial radius. Because the specific internal energy is small and the velocity large, small errors in the velocity solution give rise to large errors in the thermodynamic variables. The boundary conditions were reflecting along all boundaries. In the absence of a "flow through" outer boundary condition, the reflecting boundary condition causes a perturbation that propagates inward, so that the isentropic solution must be evaluated in window near the origin. The calculation was run to a time of 0.5.

*CM reconstruction.* Figure 17(a) is a scatter plot of density vs. distance, and (b) is the specific internal energy on a logarithmic scale. We compare the CM reconstruction method for energy modes CE/IE (red) and TE (blue). Unlike the case for shocks in which CE and TE agreed (see the Noh problem of Section 6.1.2), here the CE and IE results are identical and both agree well with the analytic solution (black). The TE result had significant errors in both density and internal energy.

CV reconstruction. In Figure 18, we compare the baseline CM-CE reconstruction method (red) with CV-TE (blue). CV-IE results are similar to CM-CE and are not shown. The CV-TE results have very large errors because the CV reconstruction does not guarantee monotonicity of the specific internal energy. Notice that the density errors are much larger than those of Figure 17 (a) which has a much more expanded scale.

#### 6.2.3. Kidder shell

Kidder [46, 44, 45, 66] derived a series of exact solutions for the isentropic compression of a gas. In this section, we calculate the isentropic compression of a hollow shell of gas [45]. Lagrange calculations of the problem have been published in [56, 25, 82, 62, 19] and an ALE calculation in [8]. Time-varying boundary conditions on the inner and outer surfaces cause the shell to compress. The goal of the Kidder hollow shell test problem is to assess the ability of the method to produce symmetric and non-dissipative results. The test problem is isentropic, so that no dissipation should be generated.

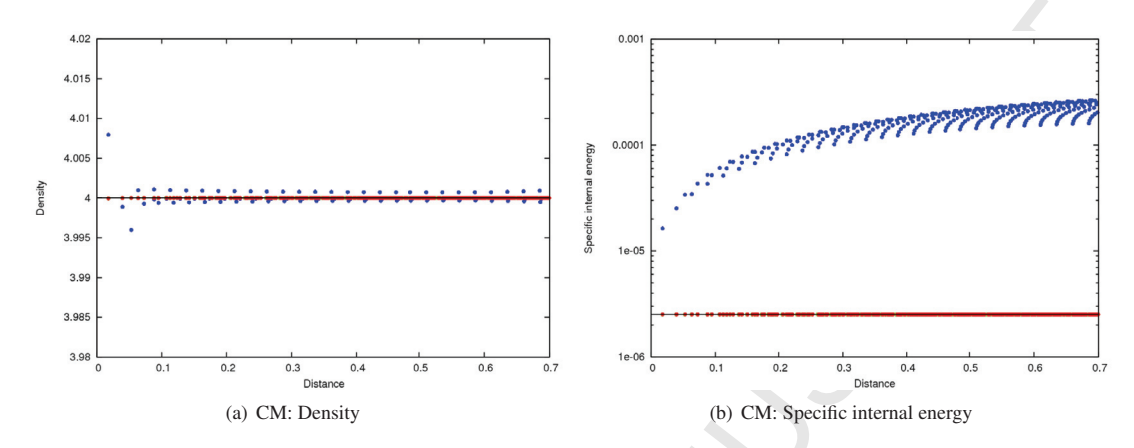


Figure 17: Coggeshall, CM reconstruction: scatter plots of density (a) and specific internal energy (b) vs. distance at t=0.5. We compare the CE/IE (red) and TE energy modes (blue). The CE and IE modes are nearly identical and agree well with the analytical result (black), but the TE result had errors in both density and internal energy.

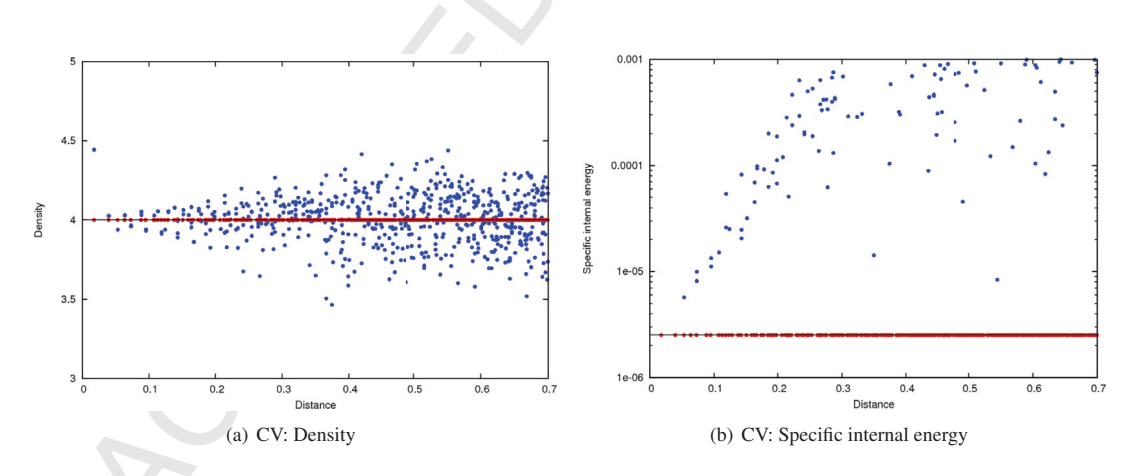


Figure 18: Coggeshall, CV reconstruction: scatter plots of density (a) and specific internal energy (b) vs. distance at t=0.5. We compare the baseline CM-CE reconstruction method (red) with CV-TE (blue). CV-IE results are similar to CM-CE and are not shown. The CV-TE results have very large errors arising from the CV reconstruction.

We ran the problem as specified in [82], but in an ALE mode because the boundaries move. The equation of state is a polytropic gas with gamma  $\gamma = \frac{\alpha+2}{\alpha}$  with  $\alpha = 1, 2, 3$  for planar, cylindrical, or spherical geometry respectively, so that  $\gamma = 2.0$  for XY geometry. Denoting the inner and outer surfaces with subscripts 1 and 2 respectively, the initial radii of the shell are  $r_1 = 0.9$  and  $r_2 = 1.0$ . The initial densities at the surfaces are  $\rho_1 = 1.0$  and  $\rho_2 = 2.0$ . The initial pressure at 1 is  $p_1 = 1.0$ . The initial distributions within the shell are given by

$$u^{0}(r) = 0$$

$$\rho^{0}(r) = \left[\rho_{1}^{\gamma-1}(1-\beta) + \beta\rho_{2}^{\gamma-1}\right]^{\frac{1}{\gamma-1}}$$

$$p^{0}(r) = \rho^{0}(r)^{\gamma}$$

$$e^{0}(r) = \frac{p^{0}(r)}{(\gamma-1)\rho^{0}(r)}$$

in which the superscript 0 denotes the initial time, and  $\beta(r) = \left(r^2 - r_1^2\right) / \left(r_2^2 - r_1^2\right)$ . The time dependent solution is self-similar, so that the radius varies as  $r(t) = r^0 \eta(t)$  in which  $\eta(t) = \sqrt{1 - \left(\frac{t}{\tau}\right)^2}$ . The focusing time  $\tau$  is the time at which the inner radius becomes zero and is given by

$$\tau = \sqrt{\frac{(\gamma - 1)\left(r_2^2 - r_1^2\right)}{2\left(c_2^2 - c_1^2\right)}}$$

in which the isentropic sound speed is  $c = \sqrt{\gamma p/\rho} = \sqrt{\gamma (\gamma - 1) e}$ . In terms of  $\eta$ , the solutions for velocity magnitude, density, pressure, and specific internal energy are given by

$$u(r,t) = r^{0} \frac{d\eta(t)}{dt} = \frac{r^{0}t}{\tau^{2}\eta(t)}$$

$$\rho(r,t) = \rho^{0}(r)\eta(t)^{\frac{-2}{\gamma-1}}$$

$$p(r,t) = p^{0}(r)\eta(t)^{\frac{-2\gamma}{\gamma-1}}$$

$$e(r,t) = \frac{p(r,t)}{(\gamma-1)\rho(r,t)}$$

For later reference, we define the average radius as  $\bar{r} = \frac{1}{n} \sum_{i=1}^{n} r_i$  and the percent RMS deviation from sphericity as

$$pct = \frac{100}{n\bar{r}} \sqrt{\sum_{i}^{n} (r_i - \bar{r})^2}$$
 (35)

with the sum being over boundary points.

We ran the problem in XY geometry, using a  $90^{\circ}$  polar mesh with 24 angular and 48 radial cells. Boundary conditions along the axes were reflecting. Time-dependent pressure boundary conditions corresponding to the above analytic solution were applied at the inner and outer radii. For this configuration,  $\tau = 0.0072648315$  and the stop time was chosen to be t = 0.005. For all reconstruction and energy methods, the average inner and outer radii closely follow the analytic solution in time as shown in Figure 19. However, as discussed below, deviations from sphericity varied between methods.

CM reconstruction. In Figure 20 we show results for CM reconstruction. Figures 20(a-c) are scatter plots of respectively velocity magnitude, density, and specific internal energy vs. distance at t = 0.005 for the 24 × 48 mesh, a size we chose to highlight some method deficiencies. We note that the 24 × 48 solution (red) differs slightly from the analytic (black) because it is not converged at this resolution. A formal convergence analysis was not done, but results for 12 × 24 (blue), 48 × 96 (purple), and 96 × 192 (green) meshes are shown in Figure 20(a). In the figure, results for the CE (red), IE, and TE modes are coincident and are in good agreement with the analytic results, aside

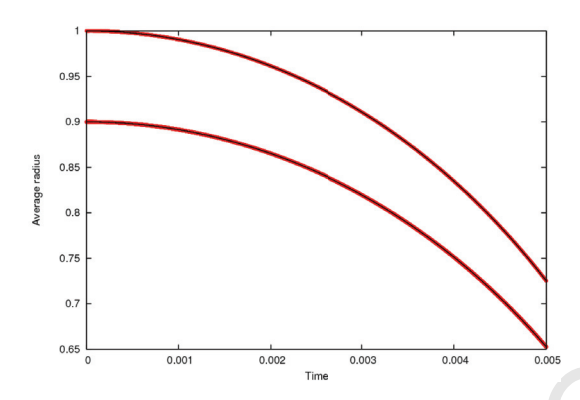


Figure 19: Kidder shell, all methods: Average radius  $\bar{r}$  vs. time

from the known convergence error. Because the specific kinetic and internal energies are much closer in value than in the Coggeshall problem, the Kidder shell problem is much less sensitive to the energy mode. In Figure 20(d), we plot the percent error in sphericity, as defined in (35), for the inner (+) and outer  $(\bullet)$  surfaces vs. time.

CV reconstruction. In Figure 21, we compare the baseline CM-CE reconstruction method (red) with the CV-IE (green) and CV-TE (blue) methods. As was the case with the Coggeshall problem, the CM-CE and CV-IE results are nearly identical for velocity magnitude, density, and specific internal energy, but the CV-TE results have large scatter. With respect to sphericity, both the CV-IE and CV-TE methods have much larger error than the baseline CM-CE.

Velocity limiter. In Figure 22, for the baseline CM-CE method, we compare the sphericity behavior of the tensor velocity limiter (red) of Section 3.3 with a simple component limiter (green) and the rotationally invariant limiter (blue). No clear winner emerges. In the Noh problem 6.1.2, the invariant limiter produced a noisy result, whereas the result on this problem is smooth (blue). It had the lowest error at the outer surface, but a larger error at the inner surface. The sphericity with the tensor limiter (red) is about a factor of three lower than the component limiter (green) over most of the time span.

#### 6.2.4. Taylor-Green vortex

This 2D problem was discussed by Taylor [74] and has been revisited by many researchers since then [31, 30, 41, 62]. The problem is of particular interest because it represents a vortical flow problem for which there is a known solution. We take our description of the problem from [30]. The material is a polytropic gas with  $\gamma = 5/3$  and unity density. The domain is a unit square with reflecting boundary conditions on each face. The initial velocity field is a counterclockwise flow about the center of the square with a magnitude given by

$$u(x, y) = \{\sin(\pi x)\cos(\pi y), -\cos(\pi x)\sin(\pi y)\}\tag{36}$$

The magnitude should remain constant in time. The initial pressure is given by

$$p(x, y) = \frac{\rho}{4} \left[ \cos(2\pi x) + \cos(2\pi y) \right] + 1$$

In addition, the problem has an energy source term because the fluid, as modeled, is compressible

$$\dot{e} = \frac{3\pi}{8} \left[ \cos(3\pi x)\cos(\pi y) - \cos(\pi x)\cos(3\pi y) \right]$$

The magnitude of the initial velocity distribution is shown in Figure 23(a) for a 60x60 mesh. The domain is 0 to 1 in both x and y directions. The velocity magnitude should remain stationary in time as in (b) that shows a Lagrangian calculation at t=0.5. Because of the large deformation, Lagrangian calculations can only be run for short times.

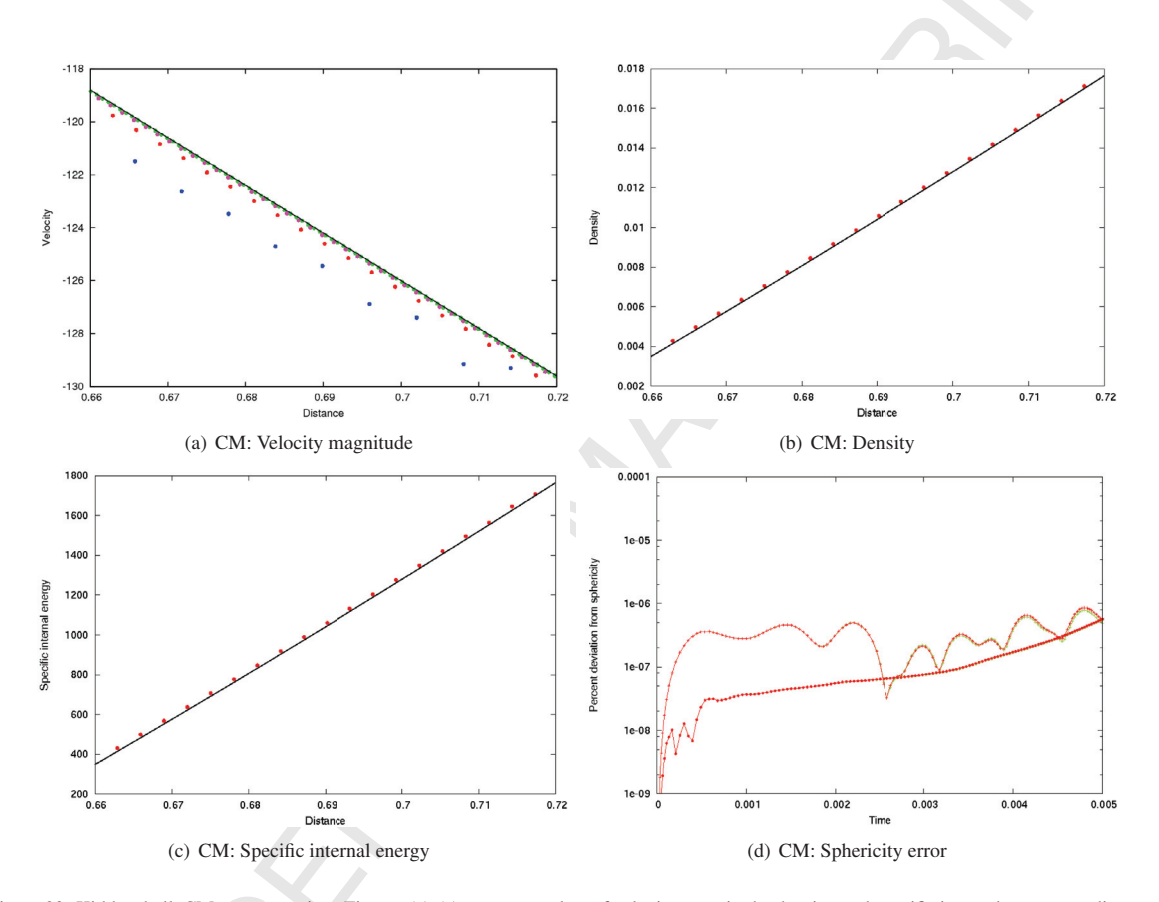


Figure 20: Kidder shell, CM reconstruction: Figures (a)-(c) are scatter plots of velocity magnitude, density, and specific internal energy vs. distance at t=t=0.005 for the  $24\times48$  mesh. CE, IE, and TE results are coincident, but only the CE (red) result is displayed. Figure (a) also shows velocity magnitude for additional mesh resolutions:  $12\times24$  (blue),  $48\times96$  (purple), and  $96\times192$  (green). Figure (d) shows percent error in sphericity, as defined in (35), for the inner (+) and outer ( $\bullet$ ) surfaces vs. time.

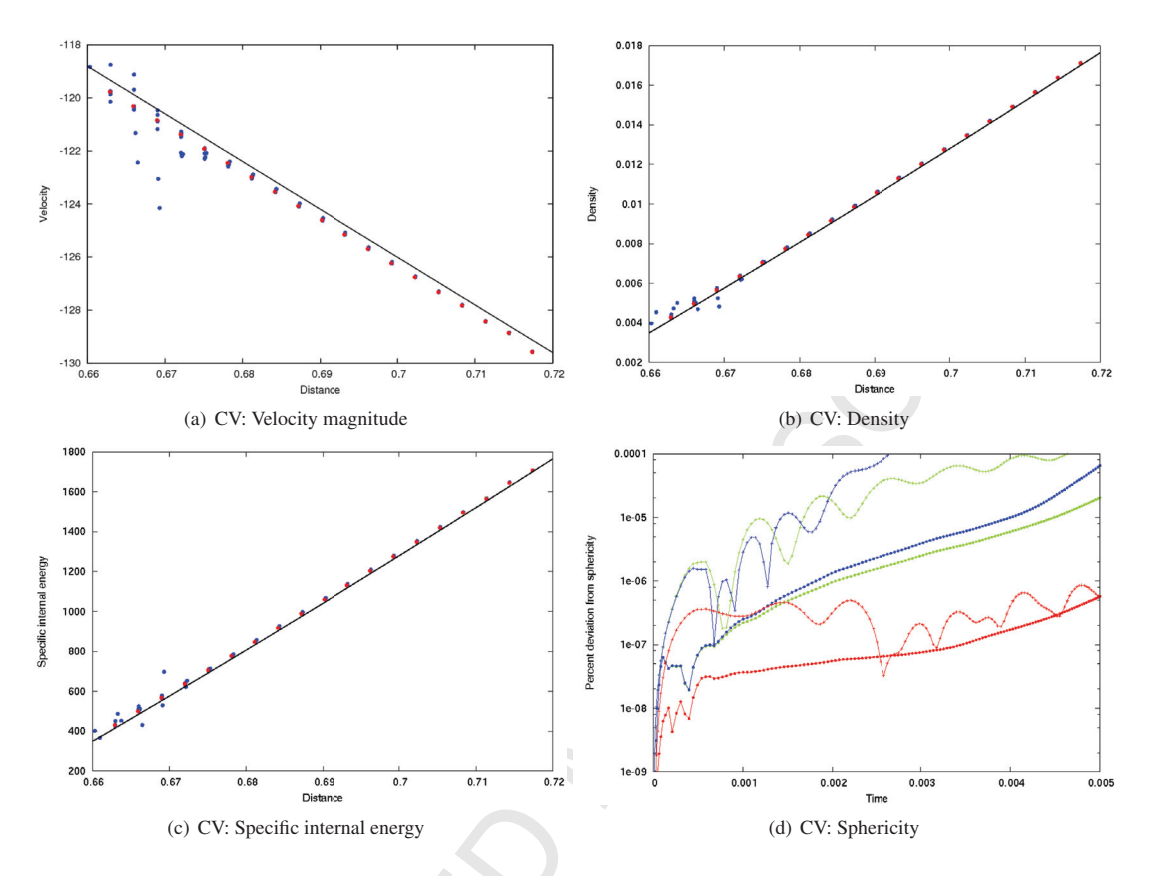


Figure 21: Kidder shell, CV reconstruction: Figures (a)-(c) are scatter plots of velocity magnitude, density, and specific internal energy vs. distance at t=t=0.005 for the  $24 \times 48$  mesh. The CM-CE (red) and CV-IE (not shown) results are nearly identical for velocity magnitude, density, and specific internal energy. The CV-TE (blue) results are scattered. Figure (d) shows percent error in sphericity, as defined in (35), for the inner (+) and outer ( $\bullet$ ) surfaces vs. time. With respect to sphericity, both the CV-IE and CV-TE methods have much larger error than the baseline CM-CE.

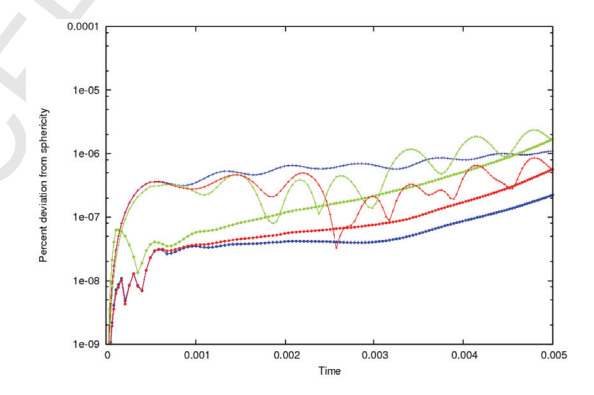


Figure 22: Kidder shell, CM reconstruction: sphericity, as defined in (35), for the inner (+) and outer (•) surfaces vs. time, comparing the tensor (red), component (green), and rotationally invariant (blue) limiters.

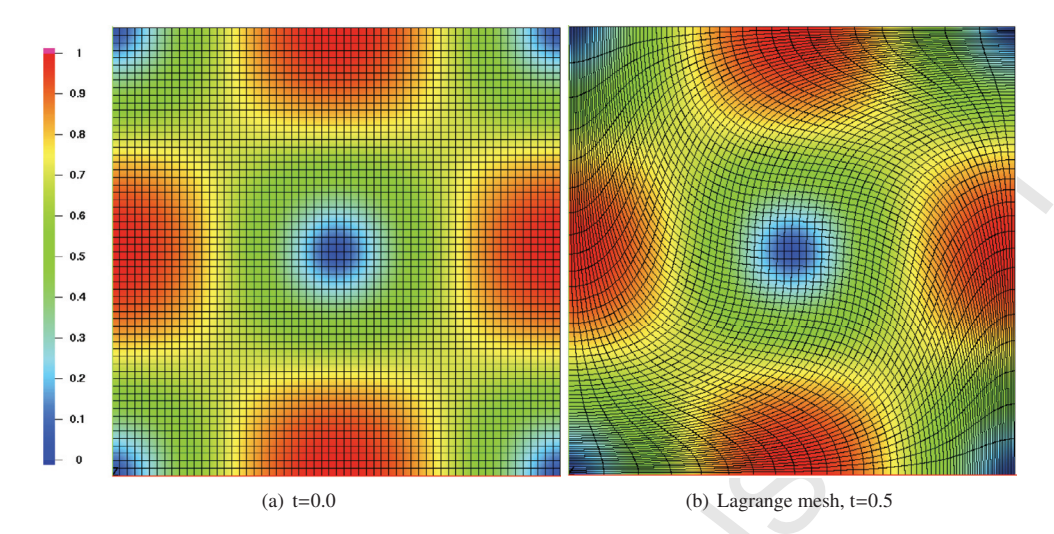


Figure 23: Taylor-Green vortex: (a) Magnitude of initial velocity field on a  $60 \times 60$  mesh on a square domain from 0 to 1. (b) Lagrangian mesh at about 1/5 revolution (t=0.5), showing stationary contours of velocity magnitude. Colors represent velocity magnitude on a scale of 0 to 1 and should remain stationary in time.

We ran the problem in an Eulerian mode at mesh resolutions of  $10 \times 10$ ,  $20 \times 20$ ,  $40 \times 40$ ,  $80 \times 80$ , and  $160 \times 160$  to a time of t = 0.5, corresponding to about 1/5 revolution. The volume-weighted L1 velocity norm is defined by

$$L1 = \frac{\sum\limits_{cells} V_{cell} \left| u_{cell} - u\left(x_c, y_c\right) \right|}{\sum\limits_{cells} V_{cell}}$$

in which  $V_{cell}$  is the cell volume,  $u_{cell}$  is the cell-centered velocity, and  $u(x_c, y_c)$  is the magnitude of velocity at the centroid  $(x_c, y_c)$  as calculated from (36).

CV reconstruction. In Figure 24(a), we plot the L1 norm of velocity magnitude vs. cell size at t = 0.5. Results from the CV (IE, TE) methods (blue) were insensitive to the energy mode. The convergence rate for the CV method varied from 2.56 to 1.68.

CM reconstruction. In Figure 24(a), we also show the L1 norm of velocity magnitude for the baseline CM (CE, IE, TE) methods (red). Results were again insensitive to the energy mode. The convergence rate for the CM method was much better than for the CV method. For the range of cell sizes tested, the rate varied from 3.01 to 2.69 which was greater than that of the underlying Lagrange hydro as reported in [19]. In Figure 24(b), we compare the CM results at t=0.5 with previously documented CM results [9] at 2.56, 5.12, 7.68, and 10.24 corresponding to 1 through 4 full revolutions. Although the absolute error increased with time, the convergence rate remained about the same.

### 6.2.5. Howell problem

Verney [81] examined the case of finite-radius, spherical copper and uranium shells collapsing under a given loading and constructed a simplified, approximate mathematical model of the problem, assuming incompressible, elastic-perfectly-plastic material response. The initial kinetic energy of the material dissipates via conversion to plastic work. These simplifications lead to a closed-form solution for the final inner radius. Later, Howell [40] considered the case of cylindrical shells. We reported results for the Lagrange case in [19]. Here, we consider only the cylindrical Howell variation.

Both variations model the collapse of a 2 cm thick Be shell. The Be is modeled as a compressible material with a density  $\rho_0 = 1.85$  g/cm<sup>3</sup>, shear modulus G = 1.51 Mb, yield strength  $Y_0 = 0.0033$  Mb, and a Gruneisen equation of state with  $c_0 = 0.7998$ , s = 1.124,  $\Gamma = 1.16$ . A detailed description of the numerical implementation of the solid model can be found in [16], Appendix A. The initial velocity magnitude distribution that drives the shell is divergence free and is

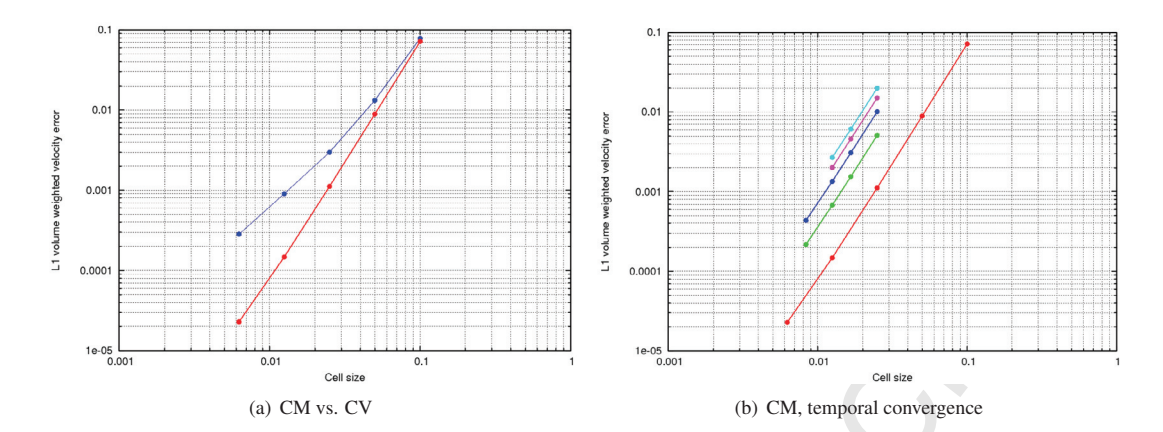


Figure 24: Taylor-Green vortex: *L*1 norm vs. cell size (the edge length of a square cell). (a) Comparison of CM (red) and CV (blue) reconstruction methods at t=0.5 or 1/5 revolution. The CM rate is nearly 3, while that of CV was much less. Points for all energy modes were coincident. (b) For CM reconstruction: *L*1 norm at 1/5 (red), 1 (green), 2 (blue), 3 (purple), and 4 (aqua) revolutions. For all times, the CM convergence rate was about 3.

given by 
$$u(r) = u_0 \left(\frac{R_{outer}}{r}\right)^{\alpha} \tag{37}$$

The initial stress state is traceless, on the yield surface, and properly rotated. The initial inner and outer radii were 8 and 10 cm respectively and the azimuthal angle was from  $0^{\circ}$  to  $180^{\circ}$ . In the XY Howell problem  $\alpha = 1.0$  and  $u_0 = 0.04902$  cm/ $\mu$ s. The shell coasts in until the kinetic energy is dissipated as plastic work. The analytic solution has a stopping time of about  $140 \, \mu$ s and an inner radius of  $4.0 \, \text{cm}$ .

Our base mesh had 16 azimuthal cells and 64 radial, but we also calculated  $4 \times 16$ ,  $8 \times 32$ ,  $32 \times 128$ , and  $64 \times 256$ . Boundary conditions are reflecting along the axis, but free on the inner and outer surfaces, requiring the problem to be run in an ALE rather than Eulerian mode.

CM and CV reconstructions. Figure 25 plots the inner radius vs. time for both reconstruction methods and all energy variations. At the resolution of Figure 25(a) all methods appear to yield a final radius of 4.0. However, the numerical solution is compressible, so that the incompressible analytic result does not hold exactly. Because the kinetic energy is not completely dissipated in the compressible calculation, the solution should oscillate about an average inner radius. Acoustic waves at a stress level less than the yield surface continue to propagate with minimal dissipation as shown in the expanded Figure 25(b). A reference Lagrange calculation (black) from [19] slightly undershoots the 4.0 value, while the ALE solutions (red) for all methods slightly overshoot. It is not until the scale is further expanded about the first minimum as in Figure 25(c) that differences in the methods become visible. The line colors are the same in all three figures, but most are not visible except in Figure 25(c): CM-CE (red), CM-IE (green), CM-TE (blue), CV-IE (purple), and CV-TE (brown). In these figures, none of the methods appear to be markedly superior to the others.

Because of the acoustic oscillations, we did not perform a conventional convergence analysis, but rather present a visual result in Figure 26 in which ALE results are shown for resolutions of  $4 \times 16$  (aqua),  $8 \times 32$  (purple),  $16 \times 64$  (blue),  $32 \times 128$  (green),  $64 \times 256$  (red). The last three resolutions are nearly coincident.

Stress limiter. In Figure 27, we compare the sphericity behavior of the baseline CM-CE method (red) using three stress limiter formulations from Section 3.3. The time interval corresponds to the time at which the greatest errors occur. In all cases, the velocity limiter was a tensor form. Results from the tensor stress limiter are red, the component limiter are green, and the rotationally invariant limiter are blue. The tensor form is marginally better than the rotationally invariant and component forms.

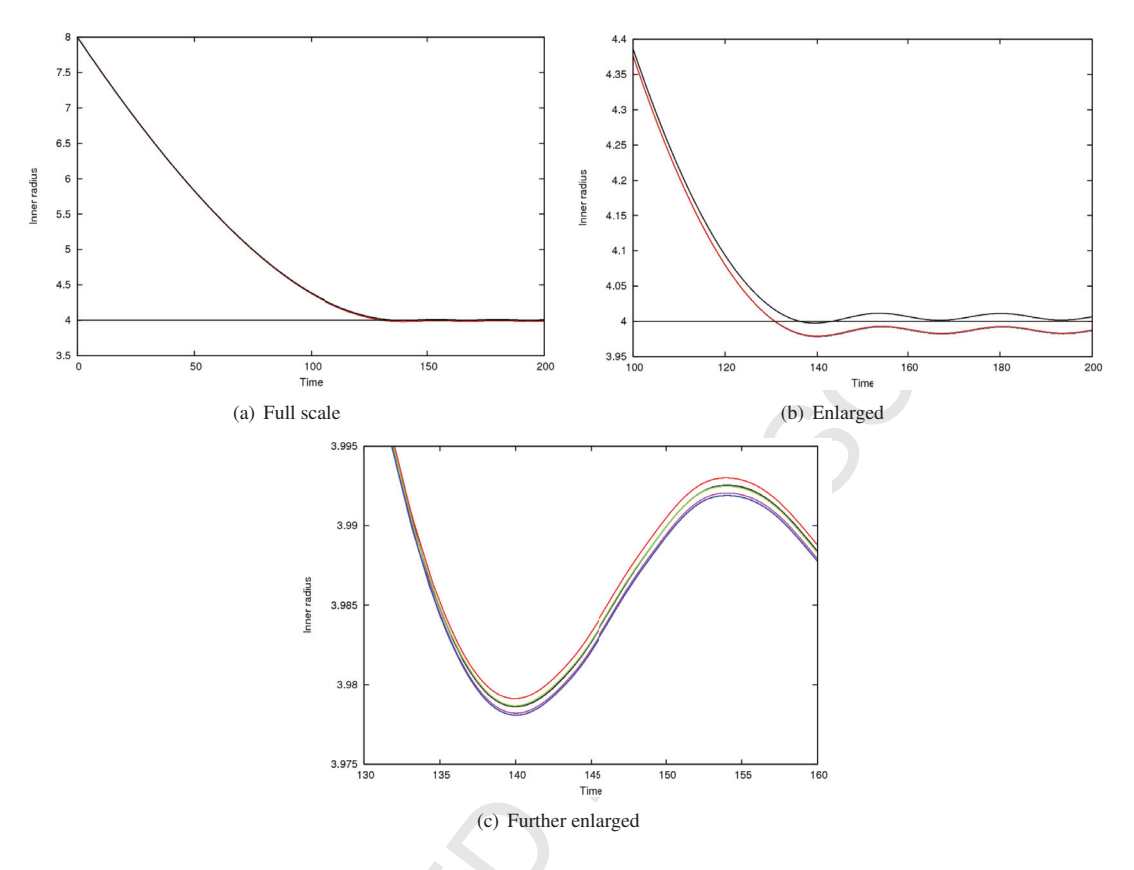


Figure 25: Howell: Inner radius vs. time for all methods for the 16×64 mesh. (a) is full scale and shows a final radius near 4.0 for all methods. (b) is enlarged to show acoustic oscillations. (c) is further enlarged about the first minimum to show the slight differences in the methods. The line colors are the same in all figures, but most are not visible except in (c): Lagrange (black), CM-CE (red), CM-IE (green), CM-TE (blue), CV-IE (purple), CV-TE (brown).

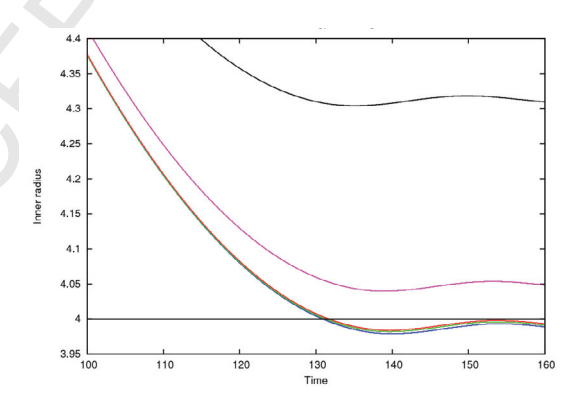


Figure 26: Howell, CM reconstruction: Inner radius vs. time for mesh resolutions of  $4 \times 16$  (black),  $8 \times 32$  (purple),  $16 \times 64$  (blue),  $32 \times 128$  (green),  $64 \times 256$  (red).

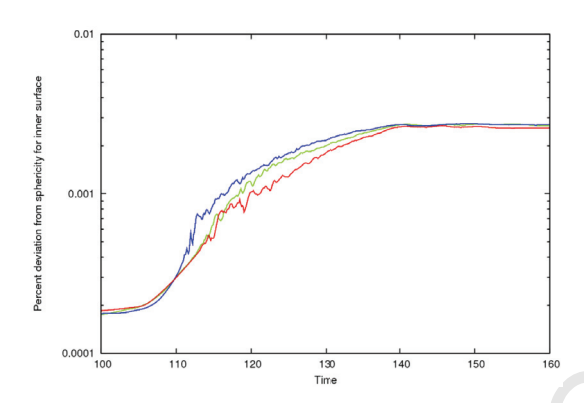


Figure 27: Howell, CM reconstruction: Percent error in sphericity, as defined in (35), vs. time for three stress limiters of Section 3.3. Tensor form (red), component form (green), rotationally invariant form (blue). Although the differences are small, the tensor form appears better.

#### 7. Summary and conclusions

The paper was presented in a context of an extended ALE scheme that permits cyclic or periodic transfer of data between grids of the same or differing connectivity. Although the overall context is more general, the focus of this paper was on the physics and numerics of the remapping of hydrodynamics fields. The new work presented falls into three categories associated with: energy conservation and entropy production, reconstruction and bounds preservation, and conservative remap of nonlinear fields.

*Energy conservation and entropy production.* Energy conservation and entropy production in Lagrangian methods has been resolved in recent years, but the solution in ALE and Eulerian methods has been elusive. This has been one of the unsolved challenges in numerical hydrodynamics, and this work has addressed some of the fundamental issues. In particular, we showed that the traditional methods of conserving either total (TE) or internal energy (IE) may not work well for both shock and smooth flow problems.

In Section 5, we presented a new compatible energy (CE) method in which total energy conservation was satisfied by conservatively and isentropically remapping internal and kinetic energy fields from the Lagrange step. The formulation included an entropy production mechanism, based upon a minimization of the Lagrangian that is constrained to retain monotonicity of the internal energy. This mechanism produced the proper entropy in shocks, while also producing no entropy in isentropic flows, as exemplified in the Coggeshall problem that is a critical test of total energy methods. A feature of the CE method is that the specific kinetic energy at the point at which the constitutive model is evaluated is always compatible with the velocity at that point. The CE method has no adjustable parameters.

The various energy schemes were sensitive to the reconstruction method that we summarize later. In Section 6, five algorithmic configurations were the focus of the testing: CM-CE, CM-IE, CM-TE, CV-IE, and CV-TE. Figure 28 is a "Stoplight" table that gives a qualitative summary of these methods on the suite of test problems. Green indicates a good result, orange a poor result, and red a markedly bad result. The left three columns compare energy modes for CM reconstruction, and the right two columns for CV reconstruction. The CE method was the only one that performed well on all problems. The IE method tended to do best on smooth flows, but failed on shocks because of conservation issues. With CM reconstruction, the TE method performed well on all but the isentropic Coggeshall problem. However, with CV reconstruction, the TE method performed poorly in all but the Howell problem because of bounds issues.

Higher order reconstruction. Canonical CV reconstruction methods are second order and linearize the product of density and specific quantities  $\rho\phi$ . The reconstruction distributes the products about the centroid. Although bounds of the products are preserved, the remapped specific fields  $\phi$  may not be. The consequences are apparent in the rightmost columns of Figure 28. Through the years, there has been an extensive literature written that aimed at improving the CV method, including such things as synchronized FCT, energy fixup schemes, energy floors, and so forth. We

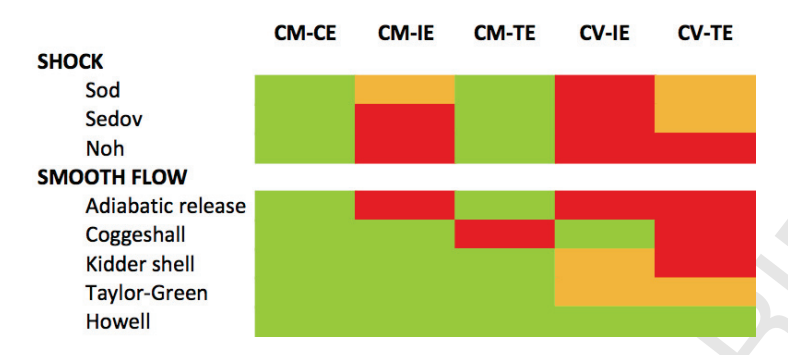


Figure 28: "Stoplight" table, a qualitative summary of test problems. Green indicates a good solution, orange a poor solution, and red a bad solution.

made no attempt to assess these extensions to CV, but rather offered an alternative scheme CM that does not have the deficiencies.

In Section 3, we described a higher order reconstruction that distributes density fields about the centroid, but specific fields about the center of mass. Although we used second order distributions for the primitive variables, their conserved products  $\rho\phi$  corresponded to higher order reconstructions. The method has the advantage that the specific fields can be easily bounded. Again, the consequences are apparent from the leftmost columns of Figure 28. A complication of the method is that the higher order polynomial distributions must be remapped.

Monotonicity is a scalar notion, and applying it in a non-directional manner to vector and tensor fields has been historically problematic. In Section 3.1, we presented three options for addressing this for both vector fields and tensor fields. These included traditional limiting of components in the global coordinate system, limiting of components in a physically relevant coordinate system through the use of a tensor limiter, and limiting of rotational invariants. The component and invariant limiters both have conceptual issues, so the tensor limiter would be expected to perform the best. The tensor limiter for velocity was better than the component limiter by about a factor of three for the Kidder Shell. Although the rotationally invariant velocity limiter did well on the Kidder Shell of Section 6.2.3, it was unacceptably bad on the box Noh problem of Section 6.1.2. Tensor limiting of the stress tensor does not appear to have been previously done. For the Howell problem of Section 6.2.5, the tensor form of the stress limiter is marginally better, and the rotationally invariant form marginally worse, with the component form in between.

Conservative remap of nonlinear fields. In Section 4, we presented a conservative remap method for mass, momentum, and total energy, as well as a pseudo conservation method for stress. The use of exact geometric intersections guarantees that the GCL is obeyed in Cartesian geometry, but axisymmetric geometry requires an additional order of polynomial integration to satisfy the GCL.

The integration of polynomial functions over polytopal intersection volumes with planar facets is critical to the CM reconstruction method. As noted, a complication of the method is that not only higher order polynomial distributions must be remapped, but also the CM itself must be located. In Cartesian geometry, third order integration is sufficient, but fourth order is required in axisymmetric geometry.

Although we limited the discussion in this paper to 2D Cartesian geometry, the remap method is readily applicable to 3D and axisymmetric geometry if the integrals are known. In 2D, volume integrals of polynomials can be expressed as surface integrals of a second polynomial. Although it is known, in principle, that for 3D the surface integral also be expressed as a line integral of a third polynomial about each facet, the details of such a method are not easily found in the literature. In Appendix A and Appendix B, we derive the necessary moment integrals to arbitrary order for these cases.

#### 8. Acknowledgments

We gratefully acknowledge the support of the U.S. Department of Energy through the LANL LDRD and ASC Programs for this work. Los Alamos National Laboratory is operated by Los Alamos National Security, LLC for the

U.S. Department of Energy NNSA under Contract No. DE-AC52-06NA25396. The Los Alamos unlimited release number of this document is: LA-UR-17-21696, version 3.

We specifically acknowledge the programmatic support of J. Brock, A. Hungerford, and M. Shashkov, as well as very useful discussions with Len Margolin, and Ted Carney. In particular, we thank Misha Shashkov for bringing [32] to our attention. We also express our appreciation to the anonymous reviewers for their very thoughtful and helpful suggestions. Acknowledgments would not be complete without recognizing the seminal contributions of John Dukowicz.

#### Appendix A. Basic integrals

Consider some volume of intersection between the donor cell and an acceptor cell. We wish to derive expressions for some basic integrals for the volume of intersection, denoted i. Coordinates  $\mathbf{x}$  are defined in a local system relative to some reference point within the donor cell located at a global position  $\mathbf{r}^0$ .

Given a polynomial expansion about the reference point

$$f(x) = f^0 + x_j f_j^1 + x_j x_k f_{jk}^2 + x_j x_k x_l f_{jkl}^3 + \dots$$

in which  $f^n_{jkl\dots}$  are expansion coefficients, the integral over the intersection volume is given by

$$F = F^{0}f^{0} + F_{i}^{1}f_{i}^{1} + F_{ik}^{2}f_{ik}^{2} + F_{ikl}^{3}f_{ikl}^{3} + \dots$$

in which expressions for the moments

$$F_{jkl...}^{n} = \int_{\cdot}^{\cdot} x_{j} x_{k} x_{l}...dA$$

are given in Appendix B. The moments are calculated as integrals about the surface of the intersection volume in the local coordinate system.

Planar geometry. In terms of these moments for 2D planar geometry, the area A and centroid  $x_j^{ev}$  evaluate to

$$A = \int dA = F^0 \tag{A.1}$$

$$Ax_j^{cv} = \int x_j dA = F_j^1 \tag{A.2}$$

In 3D, the expressions are the same with volume *V* replacing area *A*, but using 3D moment integrals.

The mass M and center of mass  $x_i^{cm}$  evaluate to

$$M = \int \rho dA \tag{A.3}$$

$$= \int \left(\rho^0 + x_j \partial_j \rho\right) dA \tag{A.4}$$

$$=F^0\rho^0 + F^1_i\partial_j\rho \tag{A.5}$$

$$Mx_j^{cm} = \int_i x_j \rho dA \tag{A.6}$$

$$= \int_{i} x_{j} \left( \rho^{0} + x_{k} \partial_{k} \rho \right) dA \tag{A.7}$$

$$=F_{i}^{1}\rho^{0}+F_{ik}^{2}\partial_{k}\rho\tag{A.8}$$

2D axial geometry. In axial geometry, extensive quantities are normalized per unit angle about the axis of rotation. The distance from the axis of rotation and any point is given by

$$r_1 = r_1^0 + x_i \delta_{i1}$$

in which the subscript 1 indicates the vector component normal to the axis. Then the volume V and centroid  $x_j^{cv}$  evaluate to

$$V = \int_{i} r dA \tag{A.9}$$

$$= \int_{\Gamma} \left( r_1^0 + x_j \delta_{j1} \right) dA \tag{A.10}$$

$$= F^0 r_1^0 + F_j^1 \delta_{j1} \tag{A.11}$$

$$Vx_j^{cv} = \int x_j r dA \tag{A.12}$$

$$= \int x_j \left( r_1^0 + x_k \delta_{k1} \right) dA \tag{A.13}$$

$$= \int \left[ x_j r_1^0 + x_j x_k \delta_{k1} \right] dA \tag{A.14}$$

$$=F_{i}^{1}r_{1}^{0}+F_{i1}^{2} \tag{A.15}$$

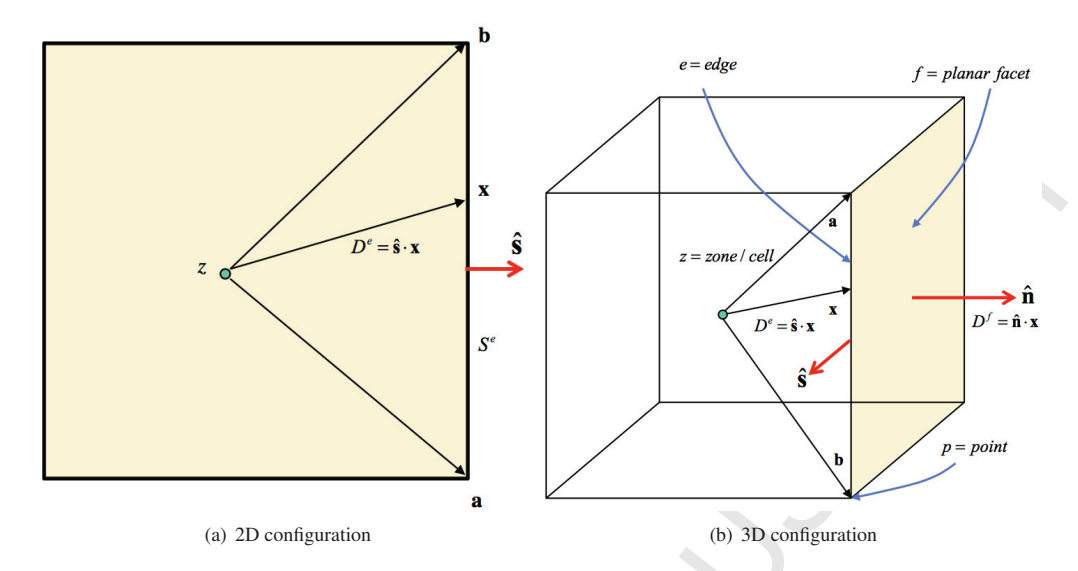


Figure A.29: Geometrical configuration in 2D(a) and 3D(b). Note that  $\hat{\mathbf{n}}$  is a unit vector normal to the facet, while  $\hat{\mathbf{s}}$  is a unit vector in the plane of the facet and normal to the edge. Although only a quadrilateral and hexahedron are depicted, the methodology applies to arbitrary polytopal volumes.

while mass M and center of mass  $x_i^{cm}$  are

$$M = \int_{\cdot} \rho r dA \tag{A.16}$$

$$= \int_{i}^{\infty} \left(\rho^{0} + x_{j}\partial_{j}\rho\right) \left(r_{1}^{0} + x_{k}\delta_{k1}\right) dA \tag{A.17}$$

$$= \int_{i} \begin{bmatrix} \left( \rho^{0} r_{1}^{0} \right) \\ + x_{j} \left( \rho^{0} \delta_{j1} + r_{1}^{0} \partial_{j} \rho \right) \\ + x_{j} x_{k} \left( \delta_{k1} \partial_{j} \rho \right) \end{bmatrix} dA$$
 (A.18)

$$= F^{0} \left( \rho^{0} r_{1}^{0} \right) + F_{1}^{1} \left( \rho^{0} \right) \tag{A.19}$$

$$+F_{j}^{1}\left(r_{1}^{0}\partial_{j}\rho\right)+F_{j1}^{2}\left(\partial_{j}\rho\right)\tag{A.20}$$

$$Mx_j^{cm} = \int_{\mathcal{X}} x_j \rho r dA \tag{A.21}$$

$$= \int_{i} \begin{bmatrix} x_{j} \left( \rho^{0} r_{1}^{0} \right) \\ + x_{j} x_{k} \left( \rho^{0} \delta_{k1} + r_{1}^{0} \partial k \rho \right) \\ + x_{j} x_{k} x_{l} \left( \delta_{l1} \partial_{k} \rho \right) \end{bmatrix} dA \qquad (A.22)$$

$$= F_{i}^{1}(\rho^{0}r_{1}^{0}) + F_{i1}^{2}(\rho^{0})$$
 (A.23)

$$+ F_{jk}^2 \left( r_1^0 \partial k \rho \right) + F_{jk1}^3 \left( \partial_k \rho \right) \tag{A.24}$$

#### Appendix B. 2D and 3D polynomial integration

We present an exact methodology for calculating 3D volume integrals of arbitrary polynomial functions over polyhedra with planar facets, as well as 2D area integrals over polygons with straight edges. Expressions for moment integrals are well known for the first 3 moments (corresponding to the volume, centroid, and moment of inertia). However, expressions for higher moments are less available.

Our methodology is derived from the divergence theorem method of Lee, Dukowicz, and others [51, 52,

34, 35, 67, 68, 61] in which the polynomial is expressed as the divergence of a second polynomial. The volume integral can then be expressed as a surface integral of the second polynomial. Although it is known, in principle, that the surface integral also be expressed as a line integral of a third function about each facet, the details of such a method are not easily found in the literature. We give explicit expressions up to the 5th moment (polynomial degree 4), and the methodology extends trivially to higher moments. Although superficially complicated, the method can be implemented with very compact code.

Appendix B.1. 2D (XY) case Consider a polynomial

$$f(x) = f^0 + x_j f_i^1 + x_j x_k f_{ik}^2 + x_j x_k x_l f_{ikl}^3 + \dots$$

in which  $f_{j...}^n$  are coefficients of a Taylor series expansion and repeated indices are summed from 1 to 3. The distances  $x_j$  are relative to some local reference point. In the 2D case, the coefficients normal to the plane are zero, so that the sum is effectively reduced to 1 to 2. Note that f could represent any component of a tensor. We wish to calculate the area integral

$$F = \int_{a}^{b} f(x) dA$$

over a polygonal cell z with planar edges. The origin is some arbitrary point about which the Taylor series is expanded, commonly the cell centroid. The geometrical configuration and notation is shown in Figure A.29(a).

It will be advantageous to express the function f in a more compact notation. Define a tensor  $\mathbf{X}^n$  that contains all of the geometrical information

$$X^{0} = 1$$

$$X_{j}^{1} = x_{j}$$

$$X_{jk}^{2} = x_{j}x_{k}$$

etc. or

$$\mathbf{X}^n = \prod_{n} \mathbf{x}$$

in which juxtaposition of tensors is an outer product. Then

$$f(x) = \sum \mathbf{f}^n * \mathbf{X}^n$$

in which \* denotes the appropriate tensor contraction. The area integral is then given by

$$F = \int_{z} f(x) dA = \sum_{n} \mathbf{f}^{n} * \int_{z} \mathbf{X}^{n} dA$$
$$= \sum_{n} \mathbf{f}^{n} * \mathbf{F}^{n}$$

in which the moment integrals are

$$\mathbf{F}^n = \int\limits_{z} \mathbf{X}^n(\mathbf{x}) \ dA$$

These can be expressed as surface integrals

$$\mathbf{F}^n = \oint_{\mathbf{a}_n} dS \ \mathbf{\hat{s}} \cdot \mathbf{h}^n$$

providing we can find functions h such that

$$\nabla \cdot (\mathbf{h}^n) = \mathbf{X}^n$$

In 2D, it can be readily verified that, using indicial notation,

$$\partial_i (x_i) = 2$$

$$\partial_i (x_i x_j) = (2x_j + \delta_{ij} x_i) = 3x_j$$

and so forth, so that we can write

$$\nabla \cdot \mathbf{x} = 2$$

$$\nabla \cdot (\mathbf{x}\mathbf{x}) = 3\mathbf{x}$$

$$\nabla \cdot (\mathbf{x}\mathbf{x}\mathbf{x}) = 4\mathbf{x}\mathbf{x}$$
...
$$\nabla \cdot (\mathbf{X}^{n+1}) = (n+2)\mathbf{X}^n$$

Then the desired function is

$$\mathbf{h}^n = \frac{\mathbf{x}\mathbf{X}^n}{n+2}$$

The moment integrals can then be written as a sum over cell edges

$$\mathbf{F}^{n} = \oint_{\partial z} dS \ \hat{\mathbf{s}} \cdot \mathbf{h}^{n} = \oint_{\partial z} dS \ (\hat{\mathbf{s}} \cdot \mathbf{x}) \frac{\mathbf{X}^{n}}{n+2}$$
$$= \sum_{e}^{z} \frac{D_{e}}{n+2} \int_{e} dS \ \mathbf{X}^{n}$$
$$= \sum_{e}^{z} \frac{S_{e} D_{e}}{n+2} \mathbf{K}^{n}$$

in which the sum  $\sum_{e}^{z}$  implies a counterclockwise sum of edges surrounding the cell. Denote **a** and **b** as the starting and ending points on the edge. The quantity

$$D_e = \mathbf{\hat{s}} \cdot \mathbf{x} = |\mathbf{a} \times \mathbf{b}|$$

can be shown to be the normal distance from the origin to the edge and can be factored out because it is constant along the edge. For an edge of length  $S_e$ , the K integral is

$$\mathbf{K}^{n} = \frac{1}{S_{e}} \int_{e}^{1} dS \ \mathbf{X}^{n}$$
$$= \int_{0}^{1} ds \ \mathbf{X}^{n}$$

in which  $ds = dS/S_e$ . These integrals are evaluated in Appendix B.4. Up to second order, the integral can be approximated

$$K^{n}\simeq\frac{1}{2}\left[ X^{n}\left( a\right) +X^{n}\left( b\right) \right]$$

Summary. In summary, then

$$F = \sum_{n} \mathbf{f}^{n} * \mathbf{F}^{n}$$

$$\mathbf{F}^{n} \sum_{e}^{z} \frac{S_{e} D_{e}}{n+2} \mathbf{K}^{n}$$

$$\mathbf{K}^{n} = \int_{0}^{1} ds \ \mathbf{X}^{n}$$

Appendix B.2. 2D (RZ) case

The case of axial symmetry (RZ) is addressed by modifying the polynomial coefficients. Recall that  $\mathbf{x}$  is relative to some reference point within the cell that is located at  $\mathbf{r}^0$  in global coordinates, so that  $\mathbf{r} = \mathbf{r}^0 + \mathbf{x}$  is the position in global coordinates. Designate the vector component normal to the axis of rotation by subscript 1. We wish to find the integral of

$$G = \int_{a}^{b} g(x)dA$$

in which

$$\begin{split} g\left(x\right) &= f\left(x\right) r_{1}\left(x\right) \\ &= f\left(x\right) \left(r_{1}^{0} + x_{m} \delta_{m1}\right) \\ &= \left(f^{0} r_{1}^{0}\right) + x_{j} \left(f_{j}^{1} r_{1}^{0} + f^{0} \delta_{j1}\right) \\ &+ x_{j} x_{k} \left(f_{jk}^{2} r_{1}^{0} + f_{j}^{1} \delta_{k1}\right) + \dots \\ &= g^{0} + x_{j} g_{j}^{1} + x_{j} x_{k} g_{jk}^{2} + \dots \end{split}$$

We have identified

$$g^{0} = f^{0}r_{1}^{0}$$

$$g_{j}^{1} = f_{j}^{1}r_{1}^{0} + f^{0}\delta_{j1}$$

$$g_{jk}^{2} = f_{jk}^{2}r_{1}^{0} + f_{j}^{1}\delta_{k1}$$

$$g_{j...kl}^{n} = f_{j...kl}^{n-1}r_{1}^{0} + f_{j...k}^{n-1}\delta_{l1}$$

The desired integral is then given by

$$G = \sum_{n} \mathbf{g}^{n} * \mathbf{F}^{n}$$

with  $\mathbf{F}^n$  being the moment integrals as derived for the preceding XY case.

Appendix B.3. 3D case

The geometrical configuration and notation is shown in Figure A.29(b). Note that  $\hat{\mathbf{n}}$  is a unit vector normal to a facet and that  $\hat{\mathbf{s}}$  is a unit vector normal to

an edge but in the plane of the facet. Similarly N represents an area of a facet and S refers to an edge length as in 2D. In the 3D case, the volume integral is again of the form

$$F = \int_{z} f(x) \ dV = \sum_{n} \mathbf{f}^{n} * \int_{z} \mathbf{X}^{n} \ dV$$
$$= \sum_{n} \mathbf{f}^{n} * \mathbf{F}^{n}$$

in which the moment integrals over the 3D volume are

$$\mathbf{F}^{n} = \int_{\mathcal{I}} \mathbf{X}^{n} \left( \mathbf{x} \right) \ dV$$

These 3D moments can be expressed as surface integrals over facets with outward normals  $\hat{\mathbf{n}}$ 

$$\mathbf{F}^n = \oint_{\mathbf{a}_n} dN \, \hat{\mathbf{n}} \cdot \mathbf{g}^n$$

providing we can find functions g such that

$$\nabla \cdot (\mathbf{g}^n) = \mathbf{X}^n$$

In 3D, It can be readily verified that

$$\nabla \cdot \mathbf{x} = 3$$

$$\nabla \cdot (\mathbf{x}\mathbf{x}) = 4\mathbf{x}$$

$$\nabla \cdot (\mathbf{x}\mathbf{x}\mathbf{x}) = 5\mathbf{x}\mathbf{x}$$
...
$$\nabla \cdot (\mathbf{X}^{n+1}) = (n+3)\mathbf{X}^n$$

so that such a function is

$$\mathbf{g}^n = \frac{\mathbf{x}\mathbf{X}^n}{n+3}$$

The moment integrals can then be written as a sum over faces

$$\mathbf{F}^{n} = \oint_{\partial z} dN \,\, \hat{\mathbf{n}} \cdot \mathbf{g}^{n} = \oint_{\partial z} dN \,\, (\hat{\mathbf{n}} \cdot \mathbf{x}) \, \frac{\mathbf{X}^{n} (\mathbf{x})}{n+3}$$
$$= \sum_{f}^{z} \frac{D_{f}}{n+3} \int_{f} dN \, \mathbf{X}^{n} (\mathbf{x})$$
$$= \sum_{f}^{z} \frac{D_{f} N_{f}}{n+3} \bar{\mathbf{X}}_{f}^{n}$$

in which the sum  $\sum_{f}^{z}$  implies a sum over outward facing facets surrounding the volume and

$$\bar{\mathbf{X}}_{f}^{n} = \frac{1}{N_{f}} \int_{f} dN \; \mathbf{X}^{n} \left( \mathbf{x} \right)$$

Now, we express  $\mathbf{x}$  as the sum of a normal distance to the facet  $\mathbf{d}$  and a displacement  $\mathbf{y}$  within the facet. This is analogous to the parallel axis theorem that translates the surface by a distance  $\mathbf{d}$ .

$$D_f = \mathbf{x} \cdot \hat{\mathbf{n}}$$
$$\mathbf{d} = D_f \hat{\mathbf{n}}$$
$$\mathbf{y} = \mathbf{x} - \mathbf{0}$$

Then, we must explicitly evaluate

$$\bar{\mathbf{X}}_{f}^{n} = \frac{1}{N_{f}} \int_{f} dN \; \mathbf{X}^{n} \left( \mathbf{d} + \mathbf{y} \right)$$

for each value of n

$$\begin{split} \bar{\mathbf{X}}_f^0 &= \frac{1}{N_f} \int_f dN = 1 \\ \bar{\mathbf{X}}_f^1 &= \frac{1}{N_f} \int_f dN \ (\mathbf{d} + \mathbf{y}) \\ &= \mathbf{d} + \frac{1}{N_f} \int_f dN \ \mathbf{y} \\ &= \mathbf{X}^1 \left( \mathbf{d} \right) + \bar{\mathbf{Y}}_f^1 \\ \bar{\mathbf{X}}_f^2 &= \frac{1}{N_f} \int_f dN \ (\mathbf{d} + \mathbf{y}) \left( \mathbf{d} + \mathbf{y} \right) \\ &= \frac{1}{N_f} \int_f dN \ (\mathbf{d} \mathbf{d} + \mathbf{d} \mathbf{y} + \mathbf{y} \mathbf{d} + \mathbf{y} \mathbf{y}) \\ &= \mathbf{d} \mathbf{d} + \mathbf{d} \bar{\mathbf{Y}}_f^1 + \bar{\mathbf{Y}}_f^1 \mathbf{d} + \bar{\mathbf{Y}}_f^2 \\ &= \mathbf{X}^2 \left( \mathbf{d} \right) + \dots + \bar{\mathbf{Y}}_f^n \end{split}$$

The 3D area integral on the undisplaced surface f can be expressed as a 2D surface integral about  $\partial f$ 

$$\mathbf{\bar{Y}}_{f}^{m} = \frac{1}{N_{f}} \int_{f} dN \, \mathbf{X}^{m} (\mathbf{y}) = \frac{1}{N_{f}} \oint_{\partial f} dS \, \mathbf{\hat{s}} \cdot \mathbf{h}^{m}$$

providing we can find a functions h such that

$$\nabla \cdot (\mathbf{h}^m) = \mathbf{X}^m$$

Such a function is again

$$\mathbf{h}^{m} = \mathbf{y} \frac{\mathbf{X}^{m} (\mathbf{y})}{m+2}$$

so that

$$\begin{split} \bar{\mathbf{Y}}_{f}^{m} &= \frac{1}{N_{f}} \oint_{\partial z} dS \ (\hat{\mathbf{s}} \cdot \mathbf{y}) \, \frac{\mathbf{X}^{m} (\mathbf{y})}{m+2} \\ &= \frac{1}{N_{f}} \sum_{e}^{f} \frac{D_{e}}{m+2} \int_{e} dS \ \mathbf{X}^{m} (\mathbf{y}) \\ &= \frac{1}{N_{f}} \sum_{e}^{f} \frac{D_{e} S_{e}}{m+2} \mathbf{K}^{m} (\mathbf{y}) \end{split}$$

in which

$$\mathbf{K}^{m}(\mathbf{y}) = \int_{0}^{1} ds \, \mathbf{X}^{m}(\mathbf{y})$$

and

$$D_e S_e = |\mathbf{a} \times \mathbf{b}|$$

Summary. In summary, then

$$F = \sum_{n} \mathbf{f}^{n} * \mathbf{F}^{n}$$

$$\mathbf{F}^{n} = V_{z} \bar{\mathbf{X}}_{z}^{n}$$

$$\bar{\mathbf{X}}_{z}^{n} = \frac{1}{V_{z}} \sum_{f}^{z} \frac{D_{f} N_{f}}{n+3} \bar{\mathbf{X}}_{f}^{n}$$

$$\bar{\mathbf{X}}_{f}^{n} = \mathbf{X}^{n} (\mathbf{d}) + \dots + \bar{\mathbf{Y}}_{f}^{n}$$

$$\bar{\mathbf{Y}}_{f}^{m} = \frac{1}{N_{f}} \sum_{e}^{f} \frac{D_{e} S_{e}}{m+2} \mathbf{K}^{m}$$

$$\mathbf{K}^{m} = \int_{0}^{1} ds \ \mathbf{X}^{m} (\mathbf{y})$$

Appendix B.4. Evaluation of K integrals

It only remains to evaluate the K integrals

$$\mathbf{K}^{n} = \int_{0}^{1} ds \; \mathbf{X}^{n} \left( \mathbf{x} \right)$$

in which  $ds = dS/S_e$ , so that  $s \in [0, 1]$ . Denoting **a** and **b** as the starting and ending points of a line segment

$$\mathbf{x} = \mathbf{a} + s(\mathbf{b} - \mathbf{a})$$
$$= \mathbf{a}(1 - s) + s\mathbf{b}$$

This can be written in terms of Bernstein polynomials, [61] that are defined by

$$A_k^n = s^k (1 - s)^{n - k}$$

so that

$$x_i = a_i (1 - s) + b_i s = a_i A_0^1 + b_i A_1^1$$

Bernstein polynomials have the property

$$A_i^p A_j^q = A_{i+j}^{p+q}$$

and their integral is known to be

$$L_k^n = \int_0^1 A_k^n ds = \frac{k! (n-k)!}{(n+1)!}$$

In particular

$$L_k^1 = \frac{1}{2!} \{1, 1\}$$

$$L_k^2 = \frac{1}{3!} \{2, 1, 2\}$$

$$L_k^3 = \frac{1}{4!} \{6, 2, 2, 6\}$$

$$L_k^4 = \frac{1}{5!} \{24, 6, 4, 6, 24\}$$

and so forth.

First order (degree 0) is trivial

$$K^{0} = \int_{0}^{1} ds = \int_{0}^{1} A_{0}^{0} ds = L_{0}^{0} = 1$$

Second order (degree 1). Now, denote the starting and ending coordinates of an edge as  $\{a_i, b_i\}$ . In terms of the polynomials,

$$x_j = a_j A_0^1 + b_j A_1^1$$

so that

$$K_{j}^{1} = \int_{0}^{1} x_{j} ds$$

$$= \int_{0}^{1} \left( a_{j} A_{0}^{1} + b_{j} A_{1}^{1} \right) ds$$

$$= a_{j} L_{0}^{1} + b_{j} L_{1}^{1}$$

$$= \frac{1}{2!} \left( a_{j} + b_{j} \right)$$

Third order (degree 2). For higher orders, the recursion relation is used.

$$x_{j}x_{k} = \left(a_{j}A_{0}^{1} + b_{j}A_{1}^{1}\right)\left(a_{k}A_{0}^{1} + b_{k}A_{1}^{1}\right)$$

$$= \begin{cases} a_{j}a_{k}A_{0}^{1}A_{0}^{1} + a_{j}b_{k}A_{0}^{1}A_{1}^{1} + \\ b_{j}a_{k}A_{0}^{1}A_{1}^{1} + b_{j}b_{k}A_{1}^{1}A_{1}^{1} \end{cases}$$

$$= \begin{cases} a_{j}a_{k}A_{0}^{2} + \\ \left(a_{j}b_{k} + b_{j}a_{k}\right)A_{1}^{2} + \\ b_{j}b_{k}A_{2}^{2} \end{cases}$$

$$= a^{2}{}_{ik}A_{0}^{2} + b^{2}{}_{ik}A_{1}^{2} + c^{2}{}_{ik}A_{2}^{2}$$

in which we define superscripted coefficients that are functions of previously calculated lower order coefficients

$$a^{2}_{jk} = a_{j}a_{k}$$
$$b^{2}_{jk} = a_{j}b_{k} + b_{j}a_{k}$$

and so forth. Then

$$K_{jk}^{2} = \int_{0}^{1} x_{j}x_{k}ds$$

$$= \frac{1}{3!} \left[ a^{2}_{jk}L_{0}^{2} + b^{2}_{jk}L_{1}^{2} + c^{2}_{jk}L_{2}^{2} \right]$$

$$= \frac{1}{3!} \left[ 2a^{2}_{jk} + b^{2}_{jk} + 2c^{2}_{jk} \right]$$

Fourth order (degree 3). Similarly

$$\begin{split} x_{j}x_{k}x_{l} &= \left\{ \begin{array}{l} \left(a^{2}{}_{jk}A_{0}^{2} + b^{2}{}_{jk}A_{1}^{2} + c^{2}{}_{jk}A_{2}^{2}\right) \times \\ \left(a_{l}A_{0}^{1} + b_{l}A_{1}^{1}\right) \end{array} \right. \\ &= \left\{ \begin{array}{l} a^{2}{}_{jk}a_{l}A_{0}^{3} + \\ \left(a^{2}{}_{jk}b_{l} + b^{2}{}_{jk}a_{l}\right)A_{1}^{3} + \\ \left(c^{2}{}_{jk}a_{l} + b^{2}{}_{jk}b_{l}\right)A_{2}^{3} + \\ c^{2}{}_{jk}b_{l}A_{3}^{3} \end{array} \right. \\ &= \left\{ \begin{array}{l} a^{3}{}_{jkl}A_{0}^{3} + b^{3}{}_{jkl}A_{1}^{3} + \\ c^{3}{}_{jkl}A_{2}^{3} + d^{3}{}_{jkl}A_{3}^{3} \end{array} \right. \end{split}$$

Then

$$K_{jkl}^{3} = \int_{0}^{1} x_{j} x_{k} x_{l} ds$$

$$= \frac{1}{4!} \begin{bmatrix} a^{3}_{jkl} L_{0}^{3} + b^{3}_{jkl} L_{1}^{3} + \\ c^{3}_{jkl} L_{2}^{3} + d^{3}_{jkl} L_{3}^{3} \end{bmatrix}$$

$$= \frac{1}{4!} \begin{bmatrix} 6a^{3}_{jkl} + 2b^{3}_{jkl} + \\ 2c^{3}_{ikl} + 6d^{3}_{ikl} \end{bmatrix}$$

Fifth order (degree 4). Similarly

$$x_{j}x_{k}x_{l}x_{m} = \begin{cases} \begin{pmatrix} a^{3}_{jkl}A_{0}^{3} + b^{3}_{jkl}A_{1}^{3} + \\ c^{3}_{jkl}A_{2}^{3} + d^{3}_{jkl}A_{3}^{3} \end{pmatrix} \times \\ (a_{m}A_{0}^{1} + b_{m}A_{1}^{1}) \\ = \begin{cases} a^{3}_{jkl}a_{m}A_{0}^{4} + \\ (a^{3}_{jkl}b_{m} + b^{3}_{jkl}a_{m})A_{1}^{4} + \\ (b^{3}_{jkl}b_{m} + c^{3}_{jkl}a_{m})A_{2}^{4} + \\ (c^{3}_{jkl}b_{m} + d^{3}_{jkl}a_{m})A_{3}^{4} + \\ d^{3}_{jkl}b_{m}A_{4}^{4} \\ d^{4}_{jklm}A_{0}^{4} + b^{4}_{jklm}A_{1}^{4} + \\ c^{4}_{jklm}A_{3}^{4} + e^{4}_{jklm}A_{4}^{4} \end{cases}$$

Then

$$K_{jklm}^{4} = \int_{0}^{1} x_{j} x_{k} x_{l} x_{m} ds$$

$$= \frac{1}{5!} \begin{bmatrix} a^{4}_{jklm} L_{0}^{4} + b^{4}_{jklm} L_{1}^{4} + \\ c^{4}_{jklm} L_{2}^{4} + \\ d^{4}_{jklm} L_{3}^{4} + e^{4}_{jklm} L_{4}^{4} \end{bmatrix}$$

$$= \frac{1}{5!} \begin{bmatrix} 24a^{4}_{jklm} + 6b^{4}_{jklm} + \\ 4c^{4}_{jklm} + 6d^{4}_{jklm} + 24e^{4}_{jklm} \end{bmatrix}$$

#### References

- [1] F.L. Addessio, J.R. Baumgardner, J.K. Dukowicz, N.L. Johnson, B.A. Kashiwa, R.M. Rauenzahn, and C. Zemach. CAVEAT: A computer code for fluid dynamics problems with large distortion and internal slip. Technical Report LA-10613, Los Alamos National Laboratory, 1990.
- T.J. Barth. Numerical methods for conservation laws on structured and unstructured meshes. Technical Report Technical Report, VKI Lecture Series, NASA, 2003.
- [3] T.J. Barth and D.C. Jespersen. The design and application of upwind schemes on unstructured meshes. In AIAA paper 89-0366, 27th Aerospace Sciences Meeting, Reno, Nevada, 1989.
- [4] G. Bazan and R.N. Rieben. Adiabatic release test problem description. Technical Report LLNL-PRES-463883, Lawrence Livermore National Laboratory, 2010.
- [5] D.J. Benson. Computational methods in Lagrangian and Eulerian hydrocodes. Comput. Meth. in Appl. Mech. and Engr., 99:235–394, 1992.
- [6] W. Bo and M.J. Shashkov. R-adaptive reconnection-based arbitrary Lagrangian Eulerian method-R-ReALE. J. Math. Study, 48(2):125–167, 2015
- [7] J. Boris and D. Book. Flux-corrected transport. I: SHASTA, a fluid transport algorithm that works. J. Comput. Phys., 230:5199-5225, 2011.
- [8] W. Boscheri and M. Dumbser. A direct arbitrary Lagrangian-Eulerian ADER-WENO finite volume scheme on unstructured tetrahedral meshes for conservative and non-conservative hyperbolic systems in 3D. J. Comput. Phys., 275:484–523, 2014.
- [9] B.J. Brown, C. Pederson, and N.R. Morgan. Material interface evolution and semi-analytic radial piston test problems. In S.R. Runnels, editor, 2015 Final Reports from the Los Alamos National Laboratory Computational Physics Student Summer Workshop. Los Alamos National Laboratory, 2015. LA-UR-15-28038.
- [10] D.E. Burton. Conservation of energy, momentum, and angular momentum in Lagrangian staggered-grid hydrodynamics. Technical Report UCRL-JC-105926, Lawrence Livermore National Laboratory, November 1990. NECDC 1990: Nuclear Explosives Code Developers' Conference, Monterey, California, November 6-9, 1990.
- [11] D.E. Burton. Exact conservation of energy and momentum in staggered-grid hydrodynamics with arbitrary connectivity. In H.E. Trease, M.J. Fritts, and W.P. Crowley, editors, Advances in the Free Lagrange Method. Springer Verlag, NY, 1990. Lawrence Livermore National Laboratory Report UCRL-JC-I04258. June 1990.
- [12] D.E. Burton. Consistent finite-volume discretization of hydrodynamic conservation laws for unstructured grids. Technical Report UCRL-JC-118788, Lawrence Livermore National Laboratory, October 1994. NECDC 1994: Eighth Nuclear Explosives Code Developers' Conference, Las Vegas, NV, October 1994.
- [13] D.E. Burton. Multidimensional discretization of conservation laws for unstructured polyhedral grids. Technical Report UCRL-JC-118306, Lawrence Livermore National Laboratory, August 1994. SAMGOP-94: 2nd International Workshop on Analytical Methods and Process Optimization in Fluid and Gas Mechanics, VNIIEF, Holiday Base, Arzamas-16, Russia, September 10-16, 1994.
- [14] D.E. Burton. Lagrangian hydrodynamics in the FLAG code. Technical Report LA-UR-07-7547, LA-UR-07-1523, Los Alamos National Laboratory, November 2007. LLNL Workshop on Advanced Numerical Methods for Lagrangian Hydrodynamics, Livermore, November 2007.
- [15] D.E. Burton, T.C. Carney, and N.R. Morgan. On the question of area weighting in cell-centered hydrodynamics. Technical Report LA-UR-13-23155, Los Alamos National Laboratory, April 2013.
- [16] D.E. Burton, T.C. Carney, N.R. Morgan, S.K. Sambastivan, and M.J. Shashkov. A cell-centered Lagrangian Godunov-like method for solid dynamics. *Comput. Fluids*, 83:33–47, 2013.
- [17] D.E. Burton, M.A. Kenamond, T.C. Carney, N.R. Morgan, and J. Fung. A cell-centered Godunov-like ALE remap scheme (RALE). Technical Report LA-UR-12-22849, Los Alamos National Laboratory, October 2012. NECDC 2012: 2012 Nuclear Explosive Code Development Conference, Livermore, October 22-26, 2012.
- [18] D.E. Burton, M.A. Kenamond, N.R. Morgan, T.C. Carney, and M.J. Shashkov. An intersection based ALE scheme (xALE) for cell centered hydrodynamics (CCH). Technical Report LA-UR-13-26756, Los Alamos National Laboratory, August 2013. MultiMat 2013: International Conference on Numerical Methods for Multi-Material Fluid Flows, San Francisco, CA September 2-6, 2013.

- [19] D.E. Burton, N.R. Morgan, T.C. Carney, and M.A. Kenamond. Reduction of dissipation in Lagrange cell-centered hydrodynamics (CCH) through corner gradient reconstruction (CGR). J. Comput. Phys., 299:229—280, 2015. LA-UR-14-28809.
- [20] D.E. Burton, N.R. Morgan, T.C. Carney, and S.K. Sambasivan. A cell-centered Godunov-like ALE method for solid dynamics. Technical Report LA-UR-12-20613, Los Alamos National Laboratory, April 2012. The 9th International Conference on New Models and Hydrocodes for Shock Processes in Condensed Matter, London, April 2012.
- [21] D.E. Burton, N.R. Morgan, M.R.J. Charest, M.A. Kenamond, and J. Fung. Development of a compatible, energy conserving, bounds preserving remap of hydrodynamic fields in a generalized ALE scheme. Technical Report LA-UR-16-27644, Los Alamos National Laboratory, October 2016.
- [22] D.E. Burton, N.R. Morgan, M.R.J. Charest, M.A. Kenamond, and J. Fung. Development of a compatible, energy conserving, bounds preserving remap of hydrodynamic fields in a generalized ALE scheme. Technical Report LA-UR-17-20378, Los Alamos National Laboratory, January 2017.
- [23] E.J. Caramana, D.E. Burton, M.J. Shashkov, and P.P. Whalen. The construction of compatible hydrodynamics algorithms utilizing conservation of total energy. J. Comput. Phys., 146(LA-UR-97-3097):227—262, 1998.
- [24] E.J. Caramana and P.P. Whalen. Numerical preservation of symmetry properties of continuum problems. J. Comput. Phys., 141:174—198, April 1998.
- [25] G. Carré, S. Del Pino, B. Després, and E. Labourasse. A cell-centered Lagrangian hydrodynamics scheme on general unstructured meshes in arbitrary dimension. J. Comput. Phys., 228:5160—5183, 2009.
- [26] M.R. Charest, D.E. Burton, J. Pouderoux, M.J. Shashkov, and M.A. Kenamond. A regional reconnection-based arbitrary Lagrangian Eulerian method. Technical Report LA-UR-16-27761, Los Alamos National Laboratory, October 2016. Nuclear Explosives Code Development Conference (NECDC 2016), Livermore, CA.
- [27] S.V. Coggeshall and J. Meyer ter Vehn. Group-invariant solutions of multidimensional hydrodynamics. J. Math. Phys., 33:3585, 1992.
- [28] R.B. DeBar. Method in two-D Eulerian hydrodynamics. Technical Report UCID-19683, Lawrence Livermore National Laboratory, 1974. OSTI ID: 6336617.
- [29] B. Després and C. Mazeran. Lagrangian gas dynamics in two dimensions and Lagrangian systems. Arch. Rational Mech. Anal., 178:327–372, 2005.
- [30] V.A. Dobrev, T.V. Kolev, and R.N. Rieben. High-order curvilinear finite element methods for Lagrangian hydrodynamics. SIAM J. Sci. Comput., 34(5):606–641, 2012.
- [31] D. Drikakis, C. Fureby, F. Grinstein, and D. Youngs. Simulation of transition and turbulence decay in the Taylor-Green vortex. J. Turbulence, 8:1–12, 2007.
- [32] J. Dukowicz and J. Baumgardner. Incremental remapping as a transport/advection algorithm. J. Comput. Phys., 160:318-335, 2000.
- [33] J. Dukowicz and N. Padial. REMAP3D: a conservative three-dimensional remapping code. Technical Report LA-12136-MS, Los Alamos National Laboratory, 1991.
- [34] J.K. Dukowicz. Conservative rezoning (remapping) for general quadrilateral meshes. J. Comput. Phys., 54:411–424, 1984.
- [35] J.K. Dukowicz and J.W. Kodis. Accurate conservative remapping (rezoning) for arbitrary Lagrangian-Eulerian computations. SIAM J. Sci. Stat. Comput., 8:305–321, 1987.
- [36] S. Galera, P.-H. Maire, and J. Breil. A two-dimensional unstructured cell-centered multi-material ALE scheme using VOF interface reconstruction. J. Comput. Phys., 229:5755–5787, 2010.
- [37] J. Grandy. Conservative remapping and regions overlays by intersecting arbitrary polyhedra. J. Comput. Phys., 148:433-466, 1999.
- [38] G.A. Hansen, R.W. Douglass, and A. Zardecki. Mesh Enhancement: Selected Elliptic Methods, Foundations, and Applications. Imperial
- [39] C.W. Hirt, A. Amsden, and J.L. Cook. An arbitrary Lagrangian-Eulerian computing method for all flow speeds. J. Comput. Phys., 14:227—-253, 1974.
- [40] B.P. Howell and G.J. Ball. A free-Lagrange augmented Godunov method for the simulation of elastic-plastic solids. J. Comput. Phys., 175:128—167, 2002.
- [41] J.R. Kamm, J.S. Brock, S.T. Brandon, D.L. Cotrell, B. Johnson, P. Knupp, W.J. Rider, T.G. Trucano, and V.G. Weirs. Enhanced verification test suite for physics simulation codes. Technical Report LA-14379, Los Alamos National Laboratory, September 2008.
- [42] M.A. Kenamond, M. Bement, and M.J. Shashkov. Compatible, total energy conserving and symmetry preserving arbitrary Lagrangian-Eulerian hydrodynamics in 2D rz - cylindrical coordinates. *J. Comput. Phys.*, 268:154–185, 2014.
- [43] M.A. Kenamond and D.E. Burton. Exact intersection remapping of multi-material domain-decomposed polygonal meshes. Technical Report LA-UR-13-26794, Los Alamos National Laboratory, August 2013. MultiMat 2013: International Conference on Numerical Methods for Multi-Material Fluid Flows, San Francisco, CA September 2-6, 2013.
- [44] R. Kidder. Laser compression of matter: optical power and energy requirements. Nucl. Fusion, 14:797–803, 1974.
- [45] R. Kidder. Laser-driven compression of hollow shells: power requirements and stability limitations. Nucl. Fusion, 16:3–14, 1974.
- [46] R. Kidder. Theory of homogeneous isentropic compression and its application to laser fusion. Nucl. Fusion, 14:53-60, 1974.
- [47] M. Klima, M. Kucharik, and M.J. Shashkov. Local error analysis and comparison of the swept- and intersection-based remapping methods. Commun. Comput. Phys., 21:526–558, 2017.
- [48] G. Kluth and B. Després. Discretization of hyperelasticity on unstructured mesh with a cell-centered Lagrangian scheme. J. Comput. Phys., 229:9092–9118, 2010.
- [49] M. Kucharik and M.J. Shashkov. Conservative multi-material remap for staggered multi-material arbitrary Lagrangian-Eulerian methods. J. Comput. Phys., 258:268–304, 2014.
- [50] D. Kuzmin, R. Löhner, and S.Turek. Flux-corrected transport. Principles, algorithms and applications. Springer-Verlag, 2005.
- [51] Y.T. Lee and A.A.G. Aristides. Algorithms for computing the volume and other integral properties of solids. I. known methods and open issues. *Communications of the ACM*, 25:635–641, 1982.
- [52] S. Lien and J.T. Kajiya. A symbolic method for calculating the integral properties of arbitrary nonconvex polyhedra. *IEEE Computer Graphics and Applications*, 4:35–41, 1984.

- [53] R. Liska, M.J. Shashkov, P. Váchal, and B. Wendroff. Optimization-based synchronized flux-corrected conservative interpolation (remapping) of mass and momentum for arbitrary Lagrangian-Eulerian methods. J. Comput. Phys., 229:1467–1497, 2010.
- [54] R. Liska, M.J. Shashkov, P. Váchal, and B. Wendroff. Synchronized flux corrected remapping for ALE methods. Comput. Fluids, 46:312–317, 2011.
- [55] R. Loubère, P.-H. Maire, M.J. Shashkov, J. Breil, and S. Galera. ReALE: a reconnection-based arbitrary Lagrangian-Eulerian method. J. Comput. Phys., 229:4724–4761, 2010.
- [56] P.-H. Maire. A high-order cell-centered Lagrangian scheme for compressible fluid flows in two-dimensional cylindrical geometry. J. Comput. Phys., 228:6882–6915, October 2009.
- [57] P.-H. Maire, R. Abgrall, J. Breil, and J. Ovadia. A cell-centered Lagrangian scheme for two-dimensional compressible flow problems. SIAM J. Sci. Comput., 29:1781–1824, 2007.
- [58] L.G. Margolin and M.J. Shashkov. Second-order sign-preserving remapping on general grids. Technical Report LA-UR-02-525, Los Alamos National Laboratory, 2002.
- [59] L.G. Margolin and M.J. Shashkov. Second-order sign-preserving remapping on general grids. J. Comput. Phys., 184:266-298, 2003.
- [60] J.M. McGlaun, S.L. Thompson, and M.G. Elrick. CTH: A three-dimensional shock wave physics code. In Proc. 1989 Hypervelocity Impact Symp., 1989.
- [61] B. Mirtich. Fast and accurate computation of polyhedral mass properties. Journal of Graphics Tools, 1:31-50, 1996.
- [62] N.R. Morgan, J.I. Waltz, D.E. Burton, M.R. Charest, T.R. Canfield, and J.G. Wohlbier. A point-centered arbitrary Lagrangian Eulerian hydrodynamic approach for tetrahedral meshes. *J. Comput. Phys.*, 290:239–273, 2015.
- [63] W. F. Noh. Errors for calculations of strong shocks using artificial viscosity and an artificial heat flux. J. Comput. Phys., 72:78-120, 1987.
- [64] J. M. Owen, R. Rieben, F. Najjar, and J. White. Adiabatic release test problem. Technical Report LLNL-PRES-557631, Lawrence Livermore National Laboratory, 2012.
- [65] C. Pederson, B. Brown, and N. Morgan. The Sedov blast wave as a radial piston verification test. *Journal of Verification, Validation, and Uncertainty Quantification*, 1:1–9, 2016.
- [66] S. Ramsey. A class of self-similar hydrodynamic test problems. Technical Report LA-UR-10-08184, Los Alamos National Laboratory, 2010.
- [67] J.D. Ramshaw. Conservative rezoning algorithm for generalized two-dimensional meshes. J. Comput. Phys., 59:193–199, 1985.
- [68] J.D. Ramshaw. Simplified second-order rezoning algorithm for generalized two-dimensional meshes. J. Comput. Phys., 67:214–222, 1986.
- [69] S.K. Sambasivan, M.J. Shashkov, and D.E. Burton. Exploration of new limiter schemes for stress tensors in Lagrangian and ALE hydrocodes. Comput. Fluids. 83, 2013.
- [70] C. Schar and P. Smolarkiewicz. A synchronous and iterative flux-correction formalism for coupled transport equations. J. Comput. Phys., 128:101–120, 1996.
- [71] L.I. Sedov, Similarity and Dimensional Methods in Mechanics, Academic Press, 1959,
- [72] M.J. Shashkov and B. Wendroff. The repair paradigm and application to conservation laws. J. Comput. Phys., 198:1265—277, 2004.
- [73] G.A. Sod. A survey of several finite difference methods for systems of non-linear hyperbolic conservation laws. *J. Comput. Phys.*, 27:1–31, 1978
- [74] G.I. Taylor and A.E. Green. Mechanism of the production of small eddies from large ones. Proc. R. Soc. London, Series A, 158:499—521, 1937.
- [75] P.D. Thomas and C.K. Lombard. Geometric conservation law and its application to flow computations on moving grids. AIAA J., 17:1030, 1979.
- [76] J.G. Trulio and K.R.Trigger. Numerical solution of the one-dimensional hydrodynamic equations in an arbitrary time-dependent coordinate system. Technical Report UCRL-6522, Lawrence Radiation Laboratory, University of California, Berkeley, 1961.
- [77] J.G. Trulio and K.R.Trigger. Numerical solution of the one-dimensional Lagrangian hydrodynamic equations. Technical Report UCRL-6267, Lawrence Radiation Laboratory, University of California, Berkeley, 1961.
- [78] B. van Leer. Towards the ultimate conservative difference scheme, V. a second-order sequel to Godunov's method. J. Comput. Phys., 32:101, 1979.
- [79] B. van Leer. Towards the ultimate conservative difference scheme, a second-order sequel to Godunov's method. J. Comput. Phys., 135:229–248, 1997.
- [80] J. Velechovsky, J. Breil, and R. Liska. Flux corrected remapping using piecewise parabolic reconstruction for 2D cell-centered ALE methods. Int. J. Numer. Meth. Fluids, 76:575–586, 2014.
- [81] D. Verney. Évaluation de la limite Élastique du cuivre et de l'uranium par des expériences d'implosion. In Behavior of Dense Media under High Dynamic Pressures, Symposium, H.D.P., IUTAM, Paris 1967, pages 293—303. Gordon and Breach, New York, 1968.
- [82] F. Vilar, P-H. Maire, and R. Abgrall. A discontinuous Galerkin discretization for solving the two-dimensional gas dynamics equations written under total Lagrangian formulation on general unstructured grids. *Journal of Computational Physics*, 276:188–234, 2014.
- [83] J. von Neumann and R.D. Richtmyer. A method for the calculation of hydrodynamic shocks. *J. Comput. Phys.*, 21:232—237, 1950.
- [84] P.P. Whalen. Algebraic limitations on two-dimensional hydrodynamics simulations. J. Comput. Phys., 124:46—54, 1996.
- [85] M.L. Wilkins. Calculation of elastic-plastic flow. In B. Alder, S. Fernbach, and M. Rotenberg, editors, Methods of Computational Physics, volume 3. Academic Press, New York, 1964.
- [86] S.T. Zalesak. Fully multidimensional flux-corrected transport algorithms for fluids. J. Comput. Phys., 31:335, 1979.